Effect of Au Nanoparticles on Mitigating Negative Effect of Humidity on ZnO-Based Gas Sensors

by

Amirhossein Alaghmandfard

B.Sc., Sharif University of Technology, 2018

M.Sc., Sharif University of Technology, 2020

A THESIS SUBMITTED IN PARTIAL FULFILLMENT OF

THE REQUIREMENTS FOR THE DEGREE OF

MASTER OF APPLIED SCIENCE

in

THE FACULTY OF GRADUATE STUDIES

(Department of Mechanical Engineering)

THE UNIVERSITY OF VICTORIA

January 2024

Supervisory Committee

Effect of Au Nanoparticles on Mitigating Negative Effect of Humidity on ZnO-Based Gas Sensors

Amirhossein Alaghmandfard

B.Sc., Sharif University of Technology, 2018

M.Sc., Sharif University of Technology, 2020

Supervisory Committee:

Mina Hoorfar, Department of Mechanical Engineering
Supervisor

Makhsud Saidaminov, Department of Electrical and Computer Engineering
Member

Abstract

This thesis presents ZnO-based gas sensors for the detection of analytes, using Au nanoparticles to reduce the destructive effects of humidity on gas detection. The ZnO nanostructures are fabricated using the thermal decomposition method for different lengths of time and at varying temperatures. These structures are characterized by the X-ray diffraction technique, revealing the wurtzite hexagonal close-packed ZnO structures. In addition, scanning electron microscopy is employed to characterize the morphology of the synthesized ZnO structures. The results show that the length of ZnO nanostructures increases by raising the calcination temperature for 12 hours. The changes in the electrical current of the sensor are studied to determine the presence of target gases at various concentrations. The results show that the ZnO nanostructures prepared at 380 ^{o}C revealed the best response toward different humidity levels due to a higher number of oxygen vacancies, which are perfect sites to react with the target gas molecules. After selecting the best ZnO-based sensor, Au nanoparticles are sputtered onto the ZnO nanostructures with different thicknesses. Based on the results, the 0.1-nm-thick Au layer creates the best sensors to reduce the effect of humidity while demonstrating a constant response toward the target gas at different humidity levels. The sensor also shows good sensitivity and selectivity toward the triethylamine gas target with a response of 17.57, which is 62.75, 60.59, 4.81, 8.29, 4.30, 42.85, 70.28, and 292.83 times higher than the response toward Acetone, Methanol, Diethyleneamine, Benzene, Toluene, Ethanol, 1-propanol, and H_2, respectively. This sensor revealed fast response and recovery times of 9.8 s and 4.4 s, respectively and promising stability over 24 days.

Keywords: Zinc Oxide Semiconductors, Au Nanoparticles, Triethylamine, Gas Sensor, Humidity Effects

Table of Contents

Supervisory Committee *ii*

Abstract *iii*

Table of Contents *iv*

List of Figures *vi*

Lay Summary *ix*

Preface *x*

Acknowledgements *xi*

Dedication *xii*

Chapter 1: Introduction *1*

Chapter 2: Literature Review *8*

2-1. Humidity Interference Mechanism **9**

2-2. Anti-Humidity Strategies **10**

2-2-1. Physical Isolation 11

2-2-2. Working Parameter Modulation 12

2-2-3. Novel Materials Development 13

2-2-4. Algorithm Compensation 14

2-2-5. Surface Engineering 14

2-2-5-1. Adding Noble Materials 15

2-2-5-2. Adding Nanomaterials 18

2-2-5-3. Adding Hydrophilic/Hydrophobic Materials 20

2-3. Triethylamine **21**

2-4. Motivation and Objective **22**

2-5. Thesis Outline **23**

Chapter 3: Methodology *24*

3-1. Materials and Methods **25**

3-2. Zinc Oxide Preparation **25**

3-2-1. Chemical Bath Deposition 25

3-2-2. Thermal Deposition (TD) 27

3-3- Materials Characterization **28**

3-3-1. X-ray Diffraction (XRD) Patterns 29
3-3-2-X-ray Photoelectron Spectroscopy 29
3-3-3-Scanning Electron Microscopy Micrographs 30
3-3-4. Gas Sensing Measurements 30

Chapter 4: Results and Discussion ***32***

4-1. Material Characterizations **33**

4-1-1. X-ray Diffraction Patterns 33
4-1-2. Scanning Electron Microscopy 35
4-1-3. Energy Dispersive X-ray spectroscopy (EDS) 37
4-1-4. X-ray photoelectron spectroscopy (XPS) 38

4-2. Sensing Characterization **41**

4-2-1. Sensing Response of Bare ZnO Sensor 41
4-2-2. Sensing Response of Au-ZnO Sensor 43
4-2-3. Selectivity Toward TEA at RH=%70 45
4-2-4. Stability and Response/Recovery times 49
4-2-5. Calibration Plot 49

Chapter 5- Conclusion ***52***

5-1. Summary **53**

5-2. Contribution **54**

5-3. Future Work **55**

Bibliography ***57***

List of Figures

Figure 1-1. Schematics illustrating 0D–3D nanomaterial-based gas sensors and their different applications. 3

Figure 1-2. Different gas sensing materials and readout system mechanisms. 4

Figure 1-3. Different fundamental factors in gas sensing application: sensitivity, selectivity, stability, operating time, limit of detection (LOD) and power consumption. 5

Figure 1-4. Structure and harmful effects of TEA and the detection applications..... 7

Figure 2-1. Schematic of humidity sensing at the MoS2/SnO2hybridfilm 10

Figure 2-2. Different methods can be used to mitigate the adverse humidity effects on gas detections. 11

Figure 2-3-a- Sensing characteristics of WS_2/PbS sensor to 1 ppm NO2 at different humidity levels without UV-light illumination, b- Sensing characteristics of W3 sensor to 1 ppm NO2 at different humidity levels with UV-light illumination 13

Figure 2-4-a- Energy band diagram of Au/WS2. b Energy band diagram of Au/WS2 under visible light illumination. (c) The sensing mechanism of 530 nm-light assisted Au/WS2 gas sensor. 17

Figure 2-5-a-Response–time curves of ISc nanofiber sensors (operating at 25 °C) to 1 ppm TMA at 30% and 85% RH, and b-response–time curves of LISc nanofiber sensors (operating at 80 °C) to 1 ppm TMA at 30% and 85% RH. 19

Figure 3-1- Steps in fabrication ZnO nanowires, using the CBD method. 26

Figure 3-2-a- Deposited sensing materials onto the IDE, b- Coated ZnO-based sensor with different thicknesses of Au NPs. 28

Figure 3-3-a- Designed setup to have control of the humidity levels and gas concentrations, b- the correlation study between humidity in both chambers. 31

Figure 4-1- XRD measurement of ZnO NSs (a) prepared at 580 at different times (0h, 1h, 3h, 7h, 12h, 21h), and different temperatures (280 °C, 380 °C, 480 °C, 580 °C), compared with the JCPD card No. 96-230-0131. 34

Figure 4-2- XRD measurements of a- JCPD card No. 96-230-0131, b- prepared ZnO NSs at 380 °C for 12h, c- Au NPs sputtered the same ZnO NSs..... 34

Figure 4-3- High resolution of (111) Au NPs peak in Au NPs sputtered on the ZnO NSs, showing FWHM, and the peak position. 35

Figure 4-4- SEM image of synthesized ZnO NSs prepared by CBD methods from (a) cross-section (b) top-view. 36

Figure 4-5- SEM image of synthesized ZnO NSs at (a) 380 °C, (b) 480 °C, (c) 580 °C. 36

Figure 4-6-a- SEM/EDS image of ZnO prepared at 380 oC, and the EDS map of b- Zn and c- O, d- available elements, atomic number, type of the produced electron type, atomic percent and error in the atomic percent.. 37

Figure 4-7-a- SEM/EDS image of Au-ZnO NSs prepared at 380 °C, and the EDS map of b- zinc and c- oxygen, d- gold, and e- available elements, atomic number, type of the produced electron type, atomic percent and error in the atomic percent. 38

Figure 4-8-a Overview XPS of pure ZnO, and high-resolution XPS spectra of b- Zn 2p, and c- O 1s in pure ZnO sample. 39

Figure 4-9-a Overview XPS of Au-ZnO heterojunction, and high-resolution XPS spectra of b- Zn 2p, and c- O 1s, d- Au 4f in the Au-ZnO heterostructures. 40

Figure 4-10- The high-resolution spectra of a- O 1s and b-Zn 2p of ZnO NSs and Au-ZnO heterostructures. 41

Figure 4-11- Response ZnO-based sensing materials, prepared at a- 380 ºC b-480 ºC c-580 ºC for 12 h toward RH=70%. 42

Figure 4-12- Response of ZnO sensor, and ZnO-based sensor, sputtered with different thicknesses of Au NPs (0.05nm, 0.1nm, 1nm, 5nm, 10nm) toward 2000ppm of ethanol at various levels of humidity. 44

Figure 4-13-Response of AZ2 toward 2000 ppm TEA at different RH. 46

Figure 4-14- Response of 0.1nm-sputtered Au onto the ZnO sensor to different gases at 2000 ppm and RH=70%. 46

Figure 4-15a- Au-ZnO heterojunction band gap structure, b- Au-ZnO sensing materials in the air atmosphere without and c- with TEA. 47

Figure 4-16a- The sensor response to 2000 ppm TEA at RH=70% over time, b- response/recovery time for AZ2..... 49

Figure 4-17-Calibration curve for the response of the sensor at different concentrations..... 50

Lay Summary

In this thesis, a novel zinc oxide-based sensor is developed for triethylamine detection and gold nanoparticles are employed to mitigate the adverse effects of humidity. The sensor demonstrates high sensitivity, selectivity, fast response/recovery times and excellent stability for triethylamine, offering potential applications in many areas, such as the organic chemical industry, agriculture, aquaculture, and healthcare. The successful implementation of this sensor contributes to the advancement of triethylamine detection technologies. It provides a promising platform to ameliorate the detrimental impacts of humidity on gas sensing measurements.

Preface

The research presented in this thesis is the original work performed by the author. This thesis was supervised by Dr. Mina Hoorfar at the Microfluidics and Nanotechnology (MiNa) laboratory in the Faculty of Mechanical Engineering at the University of Victoria.

Acknowledgements

I would like to express my gratitude to Dr. Mina Hoorfar, my supervisor, Dr. Somayeh Fardindoost, our postdoctoral fellow, Emily Earl and Jacobe Stachowski, our lab engineers, and all graduate students in our team for providing me with excellent support throughout this journey.

Dedication

This dissertation is dedicated to my Mom, Dad, and my siblings whom their unlimited love, support, and encouragement nourished my soul and inspired me to pursue my dreams.

Chapter 1: Introduction

Gas sensing plays a crucial role in various fields, including environmental monitoring, food quality and safety, industrial processes, medical diagnostics, and safety applications [1]. In the field of gas sensing, researchers have explored various materials to enhance the performance and functionality of sensors (Figure 1-1). Metal-based materials like metal-organic frameworks (MOFs) or metal oxide semiconductors (MOSs), 2D materials or graphene-like materials such as graphene or graphitic carbon nitride (g-C_3N_4), polymers, and composites are among the materials commonly investigated for gas sensing applications [2]–[7].

Each sensing material possesses unique properties that make it suitable for specific sensing requirements. MOSs, such as titanium oxide (TiO_2) and zinc oxide (ZnO), have gained considerable attention in gas sensing due to their desirable characteristics. Metal oxides offer a low-cost solution for gas sensing due to the abundance and availability of the materials used. Additionally, MOSs exhibit high sensitivity toward various gases, enabling their effective detection and monitoring. Furthurmore, MOSs demonstrate good stability, allowing for prolonged and reliable operation in diverse environmental conditions. One of the most well-known MOSs, used for gas sensing in ZnO [8]. ZnO has a wide bandgap with excellent electrical and optical properties, making it an ideal candidate for gas sensing applications [8], [9]. The energy bandgap of ZnO is around 3.3 eV, showing promising semiconducting behaviour. Furthermore, ZnO nanostructures exhibit a large surface-to-volume ratio and excellent electrical properties such as high electron mobility [9]. These properties contribute to the enhanced gas-sensing performance of ZnO-based sensors. The large surface area of ZnO allows for more gas adsorption sites, leading to increased sensitivity [9]. Additionally, the high electron mobility facilitates rapid charge transfer and response time, enabling real-time gas detection [8].

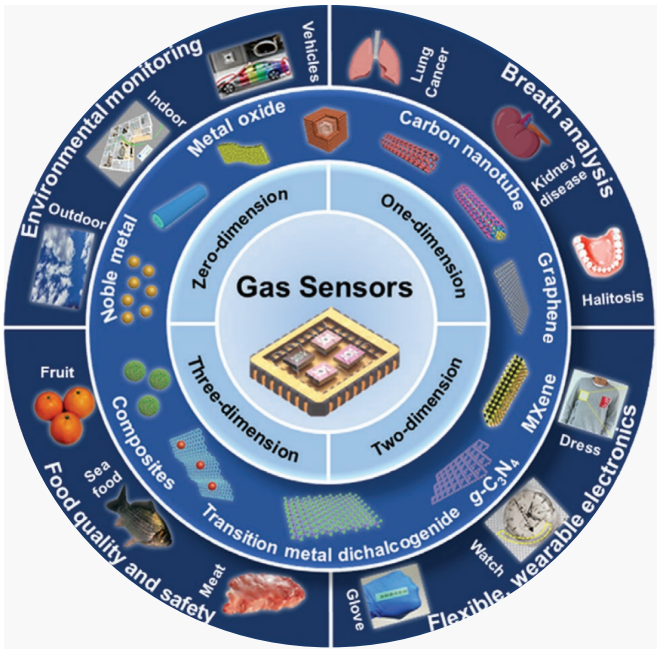

Figure 1-1- Schematics illustrating 0D–3D nanomaterial-based gas sensors and their different applications [10]**.**

Researchers focus on developing advanced gas-sensing technologies to detect and monitor different types of target gases. Gas sensing technologies can be classified into different categories based on their operating principles. These types of gas sensors include chemical sensors, electrochemical sensors, optical sensors, colorimetric sensors, acoustic sensors, etc. (Figure 1-2). However, among the various types of gas sensing techniques available, chemiresistive gas sensors have gained significant attention and are widely preferred due to their accuracy, ease of use, cost-effectiveness, and scalability for large-scale production [11], [12].

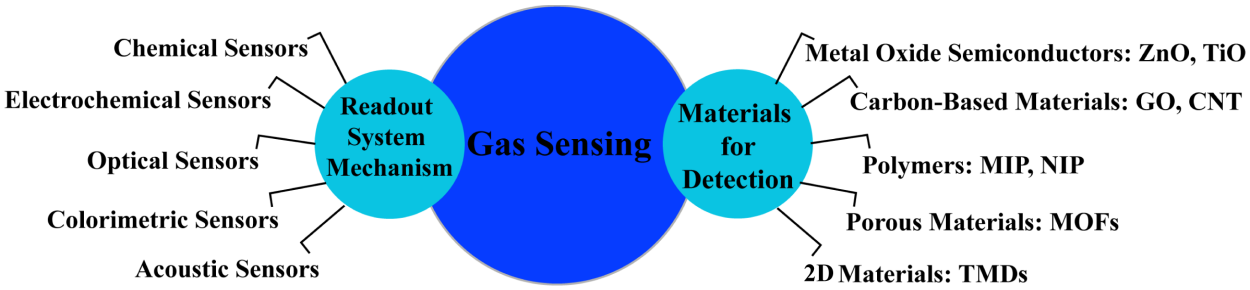

Figure 1-2- Different gas sensing materials and readout system mechanisms.

Chemiresistive gas sensors operate by measuring the change in electrical conductance or resistance of a sensing material in the presence of target molecules. The interaction between the target gas molecules and the sensing material leads to measurable changes in electrical resistance, allowing for gas detection and quantification. In gas sensing, different fundamental factors are of utmost importance: sensitivity, selectivity, stability, operating time, limit of detection (LOD) and power consumption as shown in Figure 1-3 [12]–[16]. Sensitivity refers to the ratio of the change in sensor response to the change in analyte concentration. Highly sensitive sensors are able to detect over a wide range at even low concentrations, whereas sensors that have a low sensitivity are only able to accurately detect within a narrow range and high concentrations. Selectivity denotes a sensor's capability to be sensitive to a particular gas target and distinguish it from different gases. Stability indicates a sensor's ability to maintain its performance characteristics over an extended period, including resistance to environmental variations and aging effects. Operating time refers to the time required to reach a response of 90% of the saturated state (response time) and the time required to reach 60% of the ground state (recovery time). Also, LOD refers to the lowest corresponding concentration of target gas that can be accurately detected and quantified. Finally, power consumption can be defined as the external power that is required to detect the presence of target gases in the environment.

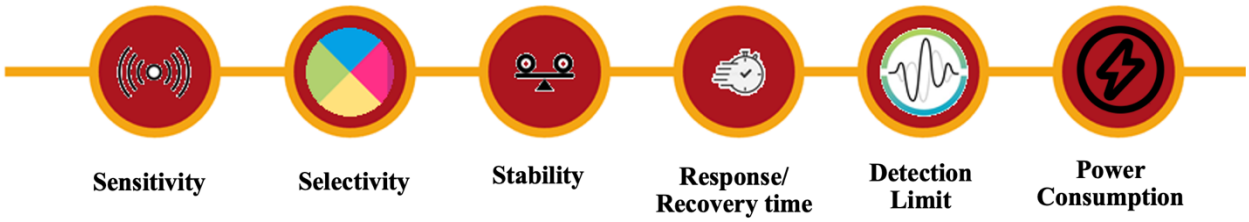

Figure 1-3- Different fundamental factors in gas sensing application: sensitivity, selectivity, stability, operating time, limit of detection and power consumption.

The performance of gas sensors is significantly influenced by various factors, including ambient environmental parameters [17]. Ambient temperature, relative humidity, and the presence of interference gases can greatly impact gas-sensing performance. Among these factors, humidity has been identified as a particularly critical parameter that affects sensor response and poses a significant challenge in gas sensing applications [18], [19]. Humidity influences the performance of chemiresistive sensors by affecting the electrical properties of the sensing material [20], [21]. When exposed to humid environments, water molecules can adsorb onto the surface of sensing materials, leading to changes in conductivity and resistance that can impact the response and accuracy of sensors. Therefore, alleviating the adverse effects humidity has on sensor response is essential for optimizing sensor performance and ensuring accurate gas detection in varying environmental conditions; however, researchers have developed various strategies to mitigate the effects of humidity and improve the reliability of gas sensors. One approach to overcoming humidity interference is by using catalysts. Catalysts can enhance gas-sensing performance by promoting specific reactions, and due to their catalytic features, they can facilitate the removal of interfering species, such as water vapour, through dissociation. Catalysts accelerate the conversion of water vapour into other products, thereby minimizing its impact on the sensing material's electrical properties. Gold (Au) is one such catalyst that has been widely employed in gas-sensing applications [22]–[24]. Au nanoparticles are known for their catalytic activity and ability to

enhance the performance of gas sensors [25]. The catalytic properties of Au nanoparticles enhance the desorption of water molecules from the sensing material's surface and dissociate them to other species, effectively reducing the impact of humidity on the sensor response. Furthermore, Au nanoparticles offer additional advantages in gas sensing since they exhibit excellent electrical conductivity and can improve charge transfer kinetics, leading to faster response times and increased sensitivity. The high surface area of gold nanoparticles also provides ample adsorption sites for gas molecules, promoting efficient gas detection.

Triethylamine (TEA) is a volatile organic compound that is mostly found or used in aquaculture, agriculture, medication development, and organic industrial chemistry [26]. This colourless and transparent gas can be used to gain information on the quality of life of marine animals, as TEA is emitted from decomposing marine animals. In addition, TEA may explode when mixed with air and comes in contact with sources of fire or flame, potentially damaging the environment and wildlife. People exposed to a high volume of TEA may experience headaches, pulmonary edema, emphysema, and more severely, death [27]. Due to the previous, the need to find an accurate and sensitive TEA sensor is one of the important areas of study many researchers are working on for gas sensing applications [28]–[30]. Figure 1-4 shows the structure, applications, and hazards of TEA.

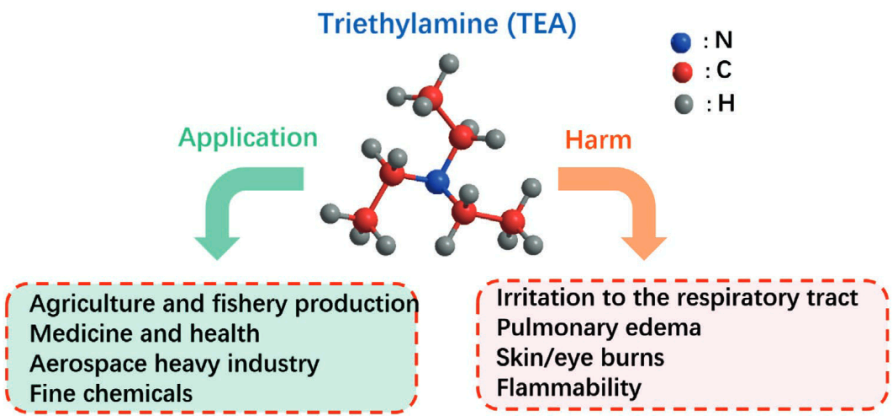

Figure 1-4- Structure and harmful effects of TEA and the detection applications [31]**.**

In this study, we aim to investigate the impact of Au nanoparticles on mitigating the effects of humidity on ZnO-based sensors for detecting TEA gas. First, the sensing materials are characterized by various techniques such as X-ray diffractometer, scanning electron microscopy, and energy dispersive spectroscopy. In the subsequent sections, we will delve deeper into the specific properties and gas-sensing characteristics of Au-ZnO chemiresistive sensors that reduce the impact of humidity, focusing on its TEA sensitivity, selectivity, and stability under varying humidity conditions. Au nanoparticles integrated within the ZnO composite serve as catalysts that facilitate the removal of water vapour and reduce its impact on the sensor's response while improving the response to TEA gas through their catalytic properties. Throughout this research, we aim to contribute to the advancement of gas sensing technologies, specifically addressing the challenges posed by humidity interference. By understanding the intricate relationship between humidity, sensor performance, and the role of gold as a catalyst, we can pave the way for the development of more accurate, reliable, and practical gas-sensing solutions in a wide range of applications.

Chapter 2: Literature Review

2-1. Humidity Interference Mechanism

One of the widely accepted sensing mechanisms for gas sensors based on MOSs is closely related to the adsorption of oxygen molecules on the sensing surface and the subsequent reactions with the electrons of the MOS to form different oxygen ion species. This adsorption results in the formation of O^{2-}, O^{-}, and O_2^{-} species, and it plays a crucial role in the gas sensing process. When gas molecules interact with these ions on the surface of MOSs, they can cause changes in the electrical properties of sensing materials leading to measurable responses [32]–[34]. In high-humidity conditions, the chemisorption and physisorption of water molecules on the surface can also induce electrical variations, causing interference with the signal. The Von Grotthuss mechanism (also known as proton hopping) is the distinct method believed to cause these variations.

The proton hopping method is a process in which hydrogen ions or protons transfer charge by diffusing through hydrogen-bonded water molecules [35]. The protons can then migrate through the crystal lattice of the MOSs, resulting in changes in the electrical conductivity of the sensors. Zhang et al. demonstrated a facile method for the fabrication of a MoS_2-modified SnO_2 hybrid nanocomposite for ultrasensitive humidity sensing [36]. Figure 2-1 shows the schematic of the humidity sensing mechanism of the MoS_2-SnO_2 hybrid film by protonic charge carriers [36]. The chemisorption and physisorption of the water molecules onto the sensor lead to the formation of a water layer [35]. The proton hopping mechanism involves the transfer of protons onto the surface of the film from one water molecule to another through hydrogen bonding. The protonic chain acts as a charge carrier which can change the electrical properties. While proton hopping plays a vital role in sensing humidity, it can affect gas-sensing performance in humid environments [35].

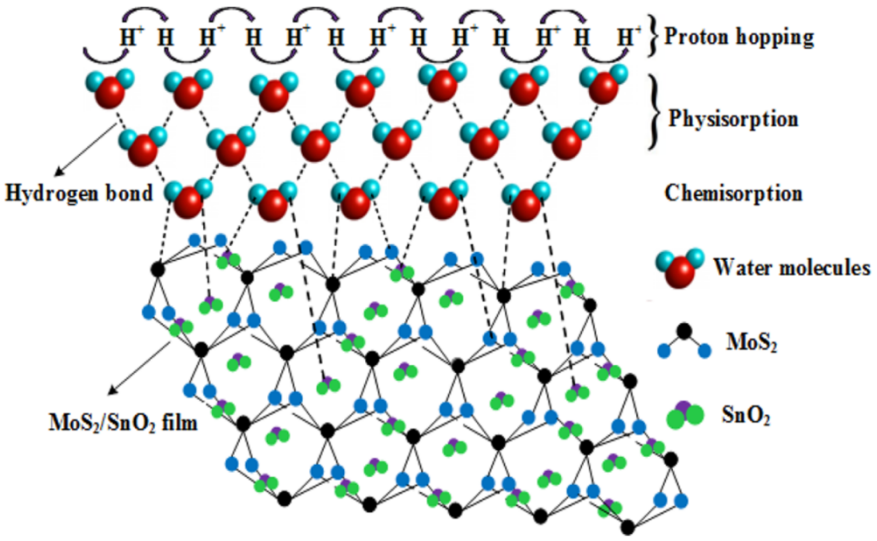

Figure 2-1- Schematic of humidity sensing of the MoS_2/SnO_2 hybrid film [35].

2-2. Anti-Humidity Strategies

To mitigate the detrimental impact of humidity on gas detection, a multitude of approaches have been used, including physical isolation, working parameter modulation, algorithm compensation, novel material development, and other related methodologies [37]; however, this research focuses on the use of surface engineering techniques (Figure 2-2).

Figure 2-2- Different methods to mitigate the effects of humidity on gas detection.

2-2-1. Physical Isolation

Recently, researchers have been working on physical isolation methods, such as the fabrication of waterproof membranes, to remove the negative impacts of humidity from other gas targets. For instance, Weber et al. developed ZnO nanostructures (NSs)-decorated with Pd NPs and a metal-organic framework, named ZIF-8 for the detection of hydrogen gas [38]. The ZIF-8 functions as a membrane, acting similar to a molecular sieve, where only molecules with kinetic diameters smaller than the window size can pass through the material [38]. Consequently, gas molecules that have kinetic diameters greater than the ZIF-8 windows (like water molecules) are unable to pass through and reach the ZnO surface [38]. As a result, tests that were done using a series of interfering molecules (all larger than H_2) did not yield any sensor response because they were unable to pass through the ZIF-8 overcoat. The superior H_2 gas selectivity of the ZIF-8/Pd/ZnO gas-sensing device can be attributed to this [38].

2-2-2. Working Parameter Modulation

The effects of humidity can be reduced by adjusting the working parameters in a variety of situations. In some circumstances, an increase in temperature can be useful in reducing the effects of humidity on gas detection [39], [40]. In addition to temperature, using different wavelengths of light to stimulate the sensing material has also been shown to reduce the impact of humidity on gas sensors [41]. A UV-light-assisted NO_2 gas sensor based on WS_2/PbS heterostructures was developed by Chen et al. [42]. They designed a gas sensor with improved anti-humidity properties and full recoverability using zero-dimensional PbS nanoparticles (NPs) and UV light [42]. They describe that the gas sensor achieves its beneficial properties for gas detection due to the use of transition metal dichalcogenides (TMDs) [42]. Scientists in this work used UV light at 365 nm to renew the gas-sensing material surface and encourage the desorption of water molecules, enhancing the sensor's ability by providing more active sites for gas adsorption [42]. It was discovered that the gas sensor's sensitivity to NO_2 gas was 1.5 times greater than that of pristine WS_2 sensors. The World Health Organization's recommended value for NO_2 in ambient air is 1 ppb, and as the gas sensor's detection limit was found to be 0.5 ppb, it is more than suitable for this application. In addition, the gas sensor demonstrated excellent NO_2 selectivity under UV light illumination with the response of 12.57 in comparison to the response of other interfering gases like NH_3, acetone, methanol, ethanol and SO_2 with 1.11, 1.10, 1.19, 1.2, 1.28, respectively [42]. The recovery time of the NO_2 gas sensor was 30 seconds and the response time was 10 seconds, suggesting that the gas sensor can detect and recover from exposure to NO_2 gas quickly [42]. Although the sensor response fluctuates in the absence of UV irradiation, a stable response can be observed from 10% to 90% relative humidity (RH) by introducing UV irradiation (Figure 2-3a, b).

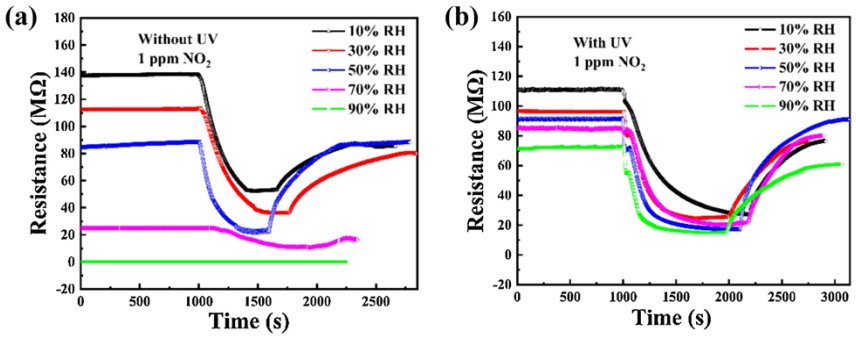

Figure 2-3-a- Sensing characteristics of WS_2/PbS sensor to 1 ppm NO2 at different humidity levels without UV-light illumination, b- Sensing characteristics of W3 sensor to 1 ppm NO2 at different humidity levels with UV-light illumination [42].

2-2-3. Novel Materials Development

Developing novel materials is also one of the effective methods to address the detrimental impacts of humidity on gas monitoring. Wu et al. created one such material, a three-dimensional graphene hydrogel with SnO_2 decorations to serve as a high-performance NO_2 gas sensor [43]. The study demonstrates how higher temperatures can effectively mitigate the detrimental impact of humidity on the sensor's reaction to NO_2 gas [43]. The response due to RH variation decreased from 30.8 to 9.9% when the temperature was raised from 22 to 54 °C. This can be explained by the fact that the increased temperature effectively removes the effects of humidity on SnO_2/RGOH, as evidenced by the fact that the response to 80% RH decreased from 5.63% to 0.2%. The decrease in humidity interference on NO_2 sensing occurs at above 54 °C, and with a 0.1 ppm detection limit, the sensor shows excellent sensitivity and selectivity toward NO_2 gas detection. Fabricating novel materials is a practical approach to removing the detrimental effects of humidity in detecting gas sensors. Qin et al. prepare precise humidity control material (PHCM) for autonomous regulation of indoor relative humidity based on metal-organic frameworks (MOFs) [44]. The MOF-PHCM structure has a high specific surface area with a high water vapor uptake of 1.62 g/g at 80% relative humidity. MOF-PHCM can autonomously control the indoor relative humidity within the desired comfort range at room temperature [44].

2-2-4. Algorithm Compensation

Algorithm compensation is a tool used by neural networks and mathematical models to compensate for the adverse humidity effects. The study, done by Mumyakmaz et al., aimed to create a reliable data processing system capable of independently measuring target gases despite changing humidity levels [45]. To achieve this, a measurement system was developed, incorporating principal component analysis (PCA) and artificial neural network (ANN) methods to compensate for humidity effects on sensor responses. The results indicated an average relative error of 1.15% in determining toluene concentrations [45].

In addition to the methods mentioned above, surface engineering has gained considerable attention amongst researchers in gas sensing applications. In this study, we primarily focus on surface engineering (in addition to aspects of working parameter modulation), including techniques such as composite formation, element doping, and modification with hydrophobic/hydrophilic materials, which will be described in detail.

2-2-5. Surface Engineering

In the realm of surface engineering, various methods have been proposed to mitigate the impact of humidity on gas detection. These techniques involve altering the composition or structure of gas-sensing materials to enhance their resistance to humidity interference. Different surface engineering techniques and modifications will be discussed in the following sections.

2-2-5-1. Adding Noble Materials

Composite formation is a widely explored approach in the field of gas sensor surface modification. It involves incorporating different materials including novel metals or elements into the sensor's composition to enhance its performance and resistance to humidity interference. Noble metals such as gold (Au), platinum (Pt), palladium (Pd), etc. have been extensively studied for their ability to improve the gas-sensing properties of materials and mitigate the diverse effects of humidity due to their catalytic impacts [46]–[52]. These catalysts, especially when used to detect gases like H_2 and VOCs, have excellent catalytic properties and can increase the surface reactions and sensitivity of gas sensors. The promotion of surface reactions enhances oxygen adsorption, resulting in the production of oxygen ions that react with target gases, increasing the sensitivity and selectivity of the sensors. For example, the incorporation of gold nanoparticles into metal oxide gas sensors has shown improved performance in terms of humidity resistance and gas detection [53]. A study on improving the responses and anti-humidity characteristics of metal oxide gas sensors was performed by Yao et. al. In this work, researchers prepared co-sensitizing gold and tin dopants with ZnO-layered porous nanocrystals [54]. The addition of Au decorations improved the sensing capabilities of the Sn-doped ZnO-layered porous nanocrystals by lessening the impact of humidity on the responses [54]. After the decoration of Au, the coefficient of variation, which was used to represent the impact of humidity on responses, dropped from 20–60% to 7–25%. The quick response and recovery characteristics were kept, and a range of operating temperatures with tolerable variation for real-world applications was studied, finding 300 degrees Celsius the optimal temperature for the accurate detection of benzene gas with different RH (with a coefficient variation of 5.70%) [54]. The study assessed the gas sensor’s response at different temperatures with four different VOCs, acetone, benzene, toluene, and m-

xylene [54]. Acetone had an optimal operating temperature of 300 ºC, while benzene, toluene, and m-xylene had an optimal operating temperature of 350 ºC [54]. The ideal operating temperature was found to be influenced by the stability of the target gas, with more stable gases requiring more thermal energy to reach their maximum response [54].

In another work, a novel gas sensor based on Au-decorated WS_2 was developed that has high sensitivity and anti-humidity properties, allowing for the detection of minute amounts of NO_2 gas at room temperature at concentrations as low as 20 ppb [55]. The formation of an H_2O film on the surface of WS_2 is prevented by the localized surface plasmon resonance (LSPR) effect of the Au nanoparticles, which encourages the dissociation of water molecules [55]. As a result, the active reaction sites that were previously occupied by water molecules become available, decreasing the impact of humidity on the gas sensor's response [55]. The catalytic action of Au nanoparticles reduces the activation energy required for gas-phase molecular reactions and improves the reaction rate, further enhancing the sensor's response [55]. Additionally, when assisted with 530 nm light, the response of the Au/WS_2 gas sensor was further improved. The interaction between the incident photons and the Au nanoparticles causes the surface electrons to oscillate, resulting in an improved sensor response towards NO_2. Au also aids in electron transfer from WS_2 (Figure 2-4a), increasing the number of electrons available for NO_2 adsorption by forming an electron accumulation layer on the Au surface [55]. The combination of Au nanoparticles and WS_2 increases the number of active NO_2 adsorption sites and improves the interactions between the sensing material and the gas molecules, which decreases the sensor's response time. In Figure 2-4a you can see the energy band diagram of the Au, WS_2, and Au/WS_2 structures without any gas exposure [55]. It displays the energy levels of the valence band (VB) and conduction band (CB) of WS_2 along with the Fermi level (EF) of Au nanoparticles and WS_2 Figure 2-4b presents the energy band diagram of the

Au/WS_2 material when illuminated with light. This diagram demonstrates how visible light excites the Au nanoparticles, resulting in electron transfer to the CB of WS_2 [55]. This process generates an electron-hole pair, which enhances gas sensing capabilities in this material. Lastly, Figure 2-4c reveals the sensing mechanism used by the 530-nm laser-assisted Au/WS_2 gas sensor. According to this diagram, visible light stimulates the Au nanoparticles, causing them to transfer electrons to the CB of WS_2. When NO_2 gas molecules are present they adsorb onto the surface of this material and alter its electrical conductivity [55].

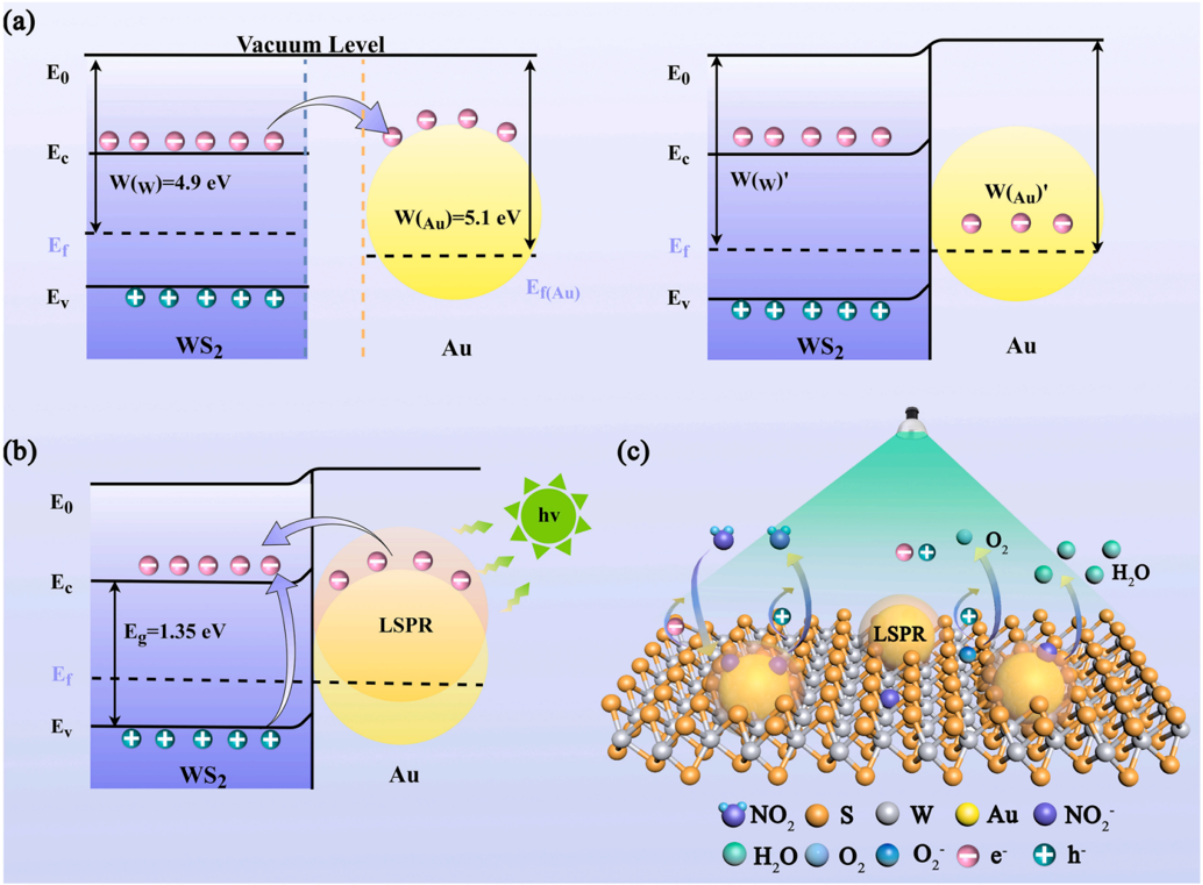

Figure 2-4-a- Energy band diagram of Au/WS_2, b- Energy band diagram of Au/WS_2 under visible light illumination, c- The sensing mechanism of 530 nm-light assisted Au/WS_2 gas sensor [55].

Haidry et al. show that Pt plays a crucial role in reducing the effects of humidity on the hydrogen sensing performance of the memristor type Pt/TiO2/Pt structure [56]. The Pt layer acts as a

protective layer that prevents the adsorption of water molecules on the TiO2 surface, which can interfere with the hydrogen sensing mechanism [56]. The Pt layer also enhances the hydrogen diffusion process through the TiO2 layer, leading to a faster response time and higher sensitivity [56]. The sensor's ability to detect hydrogen at room temperature depends heavily on the Pt/TiO2 interface because it influences how the sensor's resistance changes when exposed to hydrogen [56]. The research demonstrates that a significant resistance change is possible at the Pt/TiO2 interface, indicating the sensor's sensitivity to hydrogen [56]. Additionally, the Pt/TiO2 interface affects how Pt diffuses into the TiO2 layer, which may affect the sensor's overall performance.

2-2-5-2. Adding Nanomaterials

Nanomaterials, such as carbon nanotubes, graphene, and MOFs, have unique properties that can be harnessed to improve gas sensing performance. These nanomaterials can increase the sensor's surface area, provide additional adsorption sites for gas molecules, and enhance the sensor's response. The study done by Liu et. al. suggests an innovative method for using Ce/SnO_2 materials to improve the anti-humidity properties of MOS gas sensors [57]. At 50% humidity, the Ce/SnO_2 materials exhibit a good gas response and excellent selectivity; for 1 ppm of NO_2 at 140 °C, the response of 1 mol% Ce-doped SnO_2 sensors was 42.15. The anti-humidity mechanism is explained in terms of the regenerative oxidation/reduction reaction between Ce^{4+} and Ce^{3+} [57]. The adsorbed oxygen ions can be dynamically renewed by the CeO_2 nanoparticles on the SnO_2 sensing surface, which can maintain the concentration/configuration of adsorbed oxygen ions regardless of humidity [57].

Another research goal is focusing on creating trimethylamine (TMA) sensors with improved anti-humidity properties. TMA sensors are frequently used to assess the quality of seafood in a

variety of high-humidity environments, including supermarkets, storerooms, and springs [58]. The humidity resistance of these sensors is essential for precise and trustworthy measurements. In_2O_3-SnO_2 (IS) composite nanofibers coated with La0.7Sr0.3FeO3 (LISc) have been used to create TMA sensors [58]. The performance of LISc and IS nanofiber sensors in environments with high relative humidity was compared in the study. At 30% RH, the ISc nanofiber sensors respond with 4.2 to 1 ppm TMA, but at 85% RH, they become insensitive, meaning that the higher RH levels occupy active sites on the surface and cause a lower response toward the TMA (Figure 2-5a). This is due to the fact that In_2O_3 and SnO_2, both of which are humidity-sensing materials, only function at a temperature of 25 °C and cannot work at elevated temperatures [58]. The LISc nanofiber sensors, in contrast, show much better sensing capabilities at high humidity. At 85% RH, the responses only drop from 8.1 to 6.3, which is shown in Figure 2-5b [58]. The higher operating temperature of LISc nanofiber sensors, which lowers the concentration of water molecules around the sensors, is credited with this improvement. The coating material, La0.7Sr0.3FeO3, has excellent sensing properties even at 95% RH [58].

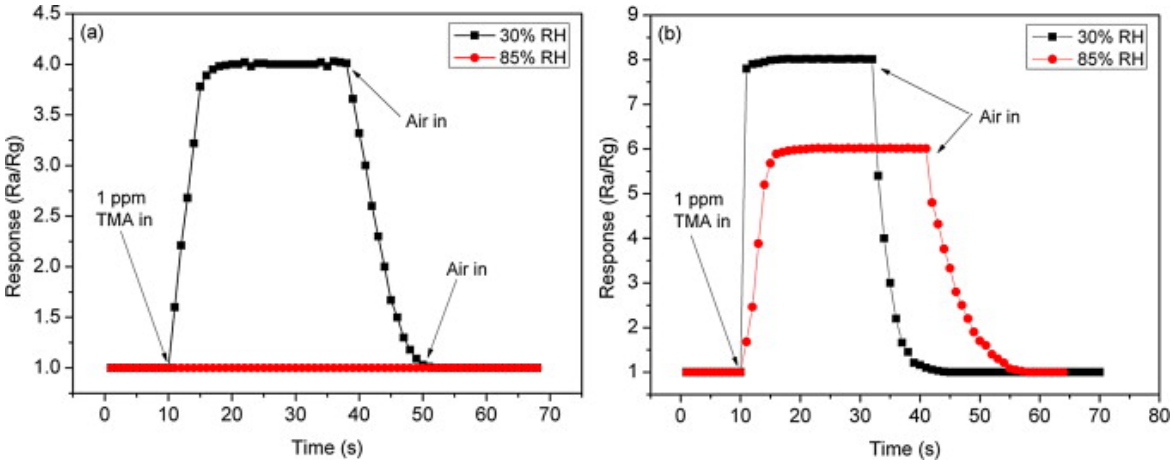

Figure 2-5-a- Response–time curves of ISc nanofiber sensors (operating at 25 °C) to 1 ppm TMA at 30% and 85% RH, and b- response–time curves of LISc nanofiber sensors (operating at 80 °C) to 1 ppm TMA at 30% and 85% Response–time curves of ISc nanofiber sensors (operating at 25 °C) to 1 ppm TMA at 30% and 85% RH, and b- response–time curves of LISc nanofiber sensors (operating at 80 °C) to 1 ppm TMA at 30% and 85% RH [58]**.**

The LISc nanofiber sensors' stability was also assessed over a 60-day period with repeated sensing measurements every 10 days. At 30% RH and 25°C, the sensors' responses to the target gases were nearly constant, demonstrating their excellent stability [58]. Overall, the anti-humidity capability of TMA sensors has been successfully improved by this work, making them suitable for precise measurements [58].

2-2-5-3. Adding Hydrophilic/Hydrophobic Materials

To control or remove water molecules and lessen the effects of humidity, hydrophilic and hydrophobic materials can also be used in two different ways to alter the surface properties of sensors. Hydrophilic materials have a strong attraction to water molecules. In contrast, water is repelled by hydrophobic substances, which causes it to bead up or roll off of the surface. The use of these materials is crucial in a variety of industries, including sensor technology, materials science, and environmental monitoring, where the presence of liquid or vapour can impair the precise operation of sensors. A common type of hydrophobic material used is Polytetrafluoroethylene. The performance of SnO2-based chemiresistive hydrogen sensors in high humidity conditions was improved by using a defect-free Teflon membrane [59]. The modified sensor displayed exceptional linearity, stability, and selectivity, particularly towards H2. The sensor consistently maintained a response of 75% to 200 ppm H2 even at 80% RH [59]. This approach is highly scalable with promising applications because of the ease of the coating technology, as well as the affordability and wide availability of commercially available Teflon [59].

Shboul et. al. describes the creation of a flexible gas sensor using hydrophobic materials like polystyrene, graphite flakes, and indium oxide [60]. The sensor proved resistant to changes in humidity and had a high sensitivity hydrogen sulfide gas at low concentrations. The sensor's

sensitivity and surface-to-volume ratio were greatly enhanced by the addition of polystyrene and graphite flakes as modifiers, creating superior sensing capabilities [60]. The manufactured sensors also displayed high stability to simulated harsh environments [60].

2-3. Triethylamine

Triethylamine (TEA) has a standard boiling point of 89.5 °C and is classified as a VOC because it contains both carbon and hydrogen atoms [26], [29]. TEA is extensively utilized in agriculture, aquaculture, aviation, medicine, and healthcare for a variety of uses, including preservation, surfactant action, organic solvent function, and catalysis [61]. TEA is prized for its many uses as a solvent and effective organocatalyst in chemical synthesis processes. It is a popular option for synthetic dyes and preservatives in industrial production due to its affordability, safety, and commercial availability. Due to its remarkable chemical and physical characteristics, it is also frequently used in chemical experiments [26]. In addition, when discharged by rotting fish and shellfish, it can also serve as a gauge of marine fish freshness. However, prolonged exposure to TEA can result in conditions like emphysema and poses serious health risks, including irritation of the skin and mucous membranes and effects on the central nervous system [29]. The National Institute for Occupational Safety and Health (NIOSH) guidelines advise maintaining indoor TEA concentration below 10 ppm. It can also cause a risk of combustion and explosion when exposed to flames, high temperatures, or potent oxidizing agents. A threshold air concentration of 1 ppm for TEA is advised by the American Conference of Governmental Industrial Hygienists and the European Commission. Therefore, there's a need for the development of sensitive TEA gas sensors with low detection limits for rapid detection [26], [29].

In recent years, there has been a notable surge in research efforts focused on TEA. This increase in attention is primarily attributed to the critical significance of detecting this analyte, marking it

as a important area of investigation. While a considerable focus of research has been conducted on TEA detection, there remain notable gaps and challenges that necessitate further exploration. One prominent concern lies in the inherent explosive nature of TEA when exposed to elevated temperatures. To effectively address this issue, the development of a sensor prototype capable of operating at lower temperatures becomes imperative. Operating at a lower temperature not only mitigates the risk of explosive reactions but also enhances the safety of the detection process. Additionally, the environmental conditions in which TEA detection may be required pose another challenge. Harsh environments characterized by high humidity levels demand a sensor that can withstand such conditions while maintaining optimal functionality. Consequently, there is an increasing need for the development of methods that can address these environmental challenges, ensuring the accuracy and reliability of TEA detection even in adverse conditions. In summary, while significant strides have been made in TEA detection research, the existing gaps underscore the need for innovative solutions. Researchers are tasked with the development of sensor prototypes capable of low-temperature operation and resilience in harsh environments. Addressing these challenges will not only enhance the safety of TEA detection processes but also contribute to the accuracy and effectiveness of analytical methodologies in diverse settings.

2-4. Motivation and Objective

My research focuses on enhancing the performance of a TEA gas detector by incorporating a gold catalyst onto a ZnO sensor. This modification aims to mitigate the negative impacts of humidity on the detector's accuracy and sensitivity. TEA detection has lots of benefits in the food industry relating to the freshness of marine creatures. Since the humidity level in fisheries is so high, there is a need to detect the emitted TEA from the rooting seafood. In addition, when this type of gas is exposed to flames, it can be caused a risk of combustion and explosion.

2-5. Thesis Outline

The synthesis of bare ZnO nanostructures and the ZnO nanostructures sputtered with Au nanoparticles, characterization methods, sensor preparation and gas sensing setup are presented in Chapter 3. Next, the materials and gas sensing characterization results are depicted in Chapter 4. At the end, a brief review of the achievements, contributions and future works are presented in Chapter 5.

Chapter 3: Methodology

3-1. Materials and Methods

In this section, a list of the main materials used in this study and where they were obtained from is presented. These materials were crucial in conducting the experiments and synthesis conducted throughout the study, and their selection was based on their properties and suitability for the intended purposes.

All chemical reactants and reagents used in this research were of analytical grade and were used as received without further purification. The zinc acetate dihydrate ($Zn(CH_3COO)_2 \cdot 2H_2O$) (ZAD), zinc nitrate hexahydrate (ZNH), and hexamethylenetetramine (HMTA) were prepared from Sigma Aldrich. The gold target (99.99%) was purchased from Kurt J. Lesker and the integrated electrodes (IDEs) with 200-micron width lines of gold were prepared by Metrohm AG. Ethanol and acetone were procured from Sigma-Aldrich, whereas toluene, 1-propanol (1-PrOH), triethylamine (TEA), and methanol were purchased from Fisher Scientific.

3-2. Zinc Oxide Preparation

ZnO nanostructures were fabricated with two different methods – chemical bath deposition (CBD) and thermal decomposition (TD). Each of these methods has advantages and disadvantages as discussed below.

3-2-1. Chemical Bath Deposition

To create the desired material on a substrate, one approach is CBD which uses a solution containing metal precursors and a reducing agent. In this project, zinc ions were reduced in the reaction to form ZnO NSs, which in this case form ZnO nanowires. The synthesis method used in this study involves the following two steps:

1. ZnO seed layer preparation: The ZnO seed layer was prepared using the sol-gel dip coating method. TEA was used as a complexing agent in a sol that contained 0.2 M of ZAD in 25 mL of 1-PrOH. The seed layers were dried after each dip coating by heating the glass substrate at 350 °C for 10 minutes. After the substrate was dip coated ten times, the substrate was calcined at 500 °C for an hour to achieve the desired thickness.
2. ZnO NSs growth: The seeded substrates were submerged in a 20 mM aqueous solution of ZNH and HMTA (acting as the precursor and reducing agent, respectively) for 3 hours at 90 °C to promote the growth of the ZnO NSs (Figure 3-1).
3. Cleaning: After the growth of the ZnO NSs, the substrate was rinsed three times, using DI water and acetone.

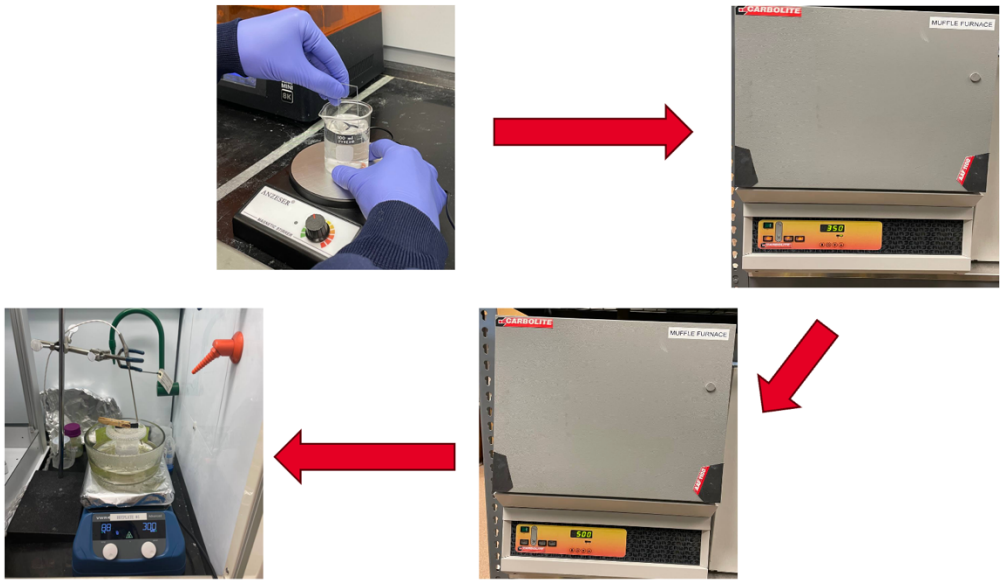

Figure 3-1- Steps in fabrication ZnO nanorods, using the CBD method.

The CBD method is an inexpensive process that produces a combination of aligned 1D nanorods and 2D nanosheets at ambient pressure; however, it requires high temperatures during synthesis and the resulting material produced is of a very small quantity. Compared to other gas-

phase techniques like pulsed laser deposition, aerosol-assisted chemical vapour deposition, and atomic layer deposition, CBD has the advantages of simplicity and low cost.

3-2-2. Thermal Deposition (TD)

The second approach used for preparing ZnO NSs is TD, which only uses a metal precursor. In this method, 5 gr of ZAD was put in a covered crucible and heated in an oven at different temperatures and for different times. Subsequently, 0.1g of synthesized ZnO NSs were dissolved into 10 ml of DI water and then deposited onto an electrode two times at a temperature of 60 ^{o}C (Figure 3-2a). The deposited sensing materials were then sputtered with Au nanoparticles with varying thicknesses (Figure 3-2b). For this research, we chose to focus on sensors sputtered with five different thicknesses, inclusive of 0.06 nm, 0.1 nm, 1 nm, 5 nm, and 10 nm, denoted as AZ1, AZ2, AZ3, AZ4, and AZ5, respectively.

The morphology that is obtained by using this method is unaligned 1D ZnO nano rods. The are several advantages for using TD compared to other methods, specifically CBD in gas sensing applications. Notably, this method offers a cheaper approach compared to the CBD method due to the reduced precursor requirement. Moreover, this method produces a powder that can be conveniently deposited onto the substrate.

Figure 3-2-a- Deposited sensing materials onto the IDE, b-coated ZnO-based sensor with different thicknesses of Au NPs.

3-3- Materials Characterization

X-ray diffraction (XRD) patterns were generated using the Empyrean PANalytical X-ray Scattering System, which uses a specific type of X-ray radiation called Cu-Kα with a wavelength of 1.54 Å. Additionally, the Hitachi S-4800 scanning electron microscope (SEM) was utilized to examine the morphology and distribution of elements in the prepared materials. For the analysis of gas sensing properties, the Multi Autolab M204 instrument was used.

In this thesis, XRD is used to understand the structure of materials and their crystallinity. By using this technique and the Debye-Sherrer formula, we can also determine the crystalline hydrodynamic size of the nanoparticles. Energy dispersive X-ray spectroscopy (EDS) and SEM are used to characterize fabricated ZnO NSs. Using EDS and SEM, the morphology, topography, nanoparticle size, and elemental distribution of a conductive specimen can be determined, which offer important information about their physical properties, especially regarding the Au NPs and their impact on the sensing materials. Several characterizations are used to relate to the gas-sensing properties of the fabricated materials. These features include sensitivity, selectivity, stability, and response and recovery times.

3-3-1. X-ray Diffraction (XRD) Patterns

A cathode ray tube generates X-rays, which are then focused towards the sample in a monochromatic beam. According to Bragg's Law ($n\lambda=2d \sin \theta$), when these incident X-rays interact with the sample, they produce a diffracted ray. Bragg's Law establishes a relationship between the lattice spacing, diffraction angle, and electromagnetic radiation wavelength in a crystalline sample. The sample is scanned through a range of 2θ angles to capture all possible diffraction directions of the lattice caused by the random orientation of the powdered material. Since every mineral has a distinct set of d-spacings, converting the diffraction peaks into d-spacings allows for the identification of materials This identification is typically accomplished by contrasting the d-spacings with accepted reference patterns. The X-ray diffraction patterns, obtained by Empyrean PANalytical X-ray Scattering System, were gained using Cu-K_α radiation. To prepare a sample for this characterization process, the materials are drop casted on a 25*25 mm^2 glass slide.

3-3-2-X-ray Photoelectron Spectroscopy

The PHI Quantera II Scanning XPS Microprobe is a highly advanced instrument designed for surface analysis, utilizing X-ray Photoelectron Spectroscopy (XPS) to provide detailed information about the composition and chemical states of materials. The instrument employs an Al-K_α X-ray source with a photon energy of 1486.6 eV, ensuring precise and efficient excitation. The X-ray beam conditions are optimized at 100 μA, 25 W, and 15 kV. The pass energy settings vary for different analyses, with 224 eV for survey scans, 112 eV for carbon (C) scans, and 26 eV for Zn and O scans. The instrument offers excellent resolution with a step size of 0.8 eV for survey scans and 0.1 eV for individual elements, enabling detailed elemental and chemical state identification.

3-3-3-Scanning Electron Microscopy Micrographs

Through the use of a focused beam of high-energy electrons from an electron microscope, various signals are produced on the surface of solid specimens. These signals, which come from interactions between the sample and electrons, reveal details about the sample's topography, chemical composition, crystalline structure, and orientation, in addition to its external appearance (such as texture). With magnification levels ranging from 20X to roughly 30,000X and a spatial resolution of 50 to 100 nm, this imaging method can cover areas with widths of approximately 1 cm to 5 microns. Specialized points on the sample can also be analyzed by the SEM, which is especially helpful for qualitative or semi-quantitative analyses of chemical compositions (using EDS) and crystalline structure and orientations (using Electron Backscatter Diffraction (EBSD)).

In this experiment, Hitachi S-4800 SEM within the Advanced Microscopy Facility at the University of Victoria was used to characterize the prepared ZnO samples. In this analysis, ZnO NSs were drop cast onto a glass substrate and coated with gold and carbon for SEM and EDS, respectively, to increase conductivity. For imaging, the accelerating voltage was set to 1 kV, and working distances in the range of 2.9 mm and 8 mm were used. Subsequently, the acquired SEM images and EDS measurements were used to analyze the morphology and size distribution of the particles, using ImageJ software.

3-3-4. Gas Sensing Measurements

To control humidity levels, an experimental setup made up of different parts was developed, shown in Figure 3-3a. Two chambers make up this setup, where a humidifier is used to create humidity in the larger one. By adjusting the humidifier to increase humidity or adding N_2 gas to decrease it, the humidity levels can be managed. The chamber's humidity is evenly distributed in the bigger chamber thanks to an integrated fan. On the left side of the larger chamber a pump was

installed to transfer moisture into the smaller chamber which houses the fabricated sensor. The sensor can be connected to a potentiostat to monitor its response. The setup uses a commercial humidity sensor to track the relative humidity, and both chambers have digital displays that show the readings. The relationship between the humidity levels in the bigger and smaller chambers was also investigated through a correlation study (see Figure 3-3b). The inset of Figure 3-3b contains the equation that describes this correlation. With this configuration, it is possible to examine how the sensor reacts to various target gases at various humidity levels.

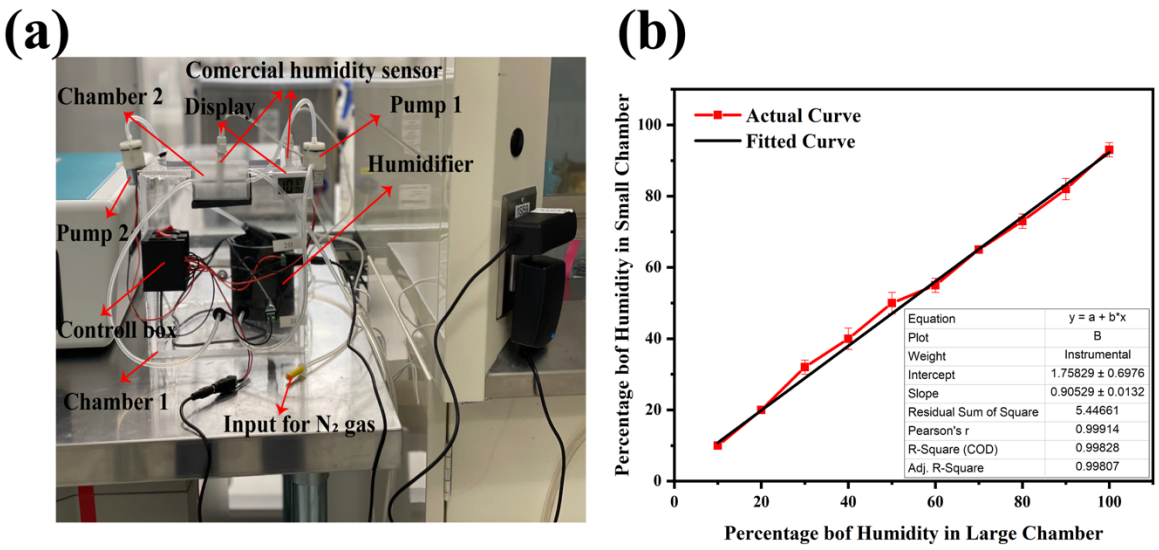

Figure 3-3-a- Designed setup to have control of the humidity levels and gas concentrations, b- the correlation study between humidity in both chambers.

Gas sensing measurement was done by using a Multi Autolab M204 potentiostat. We decided to primarily focus on the chrono amperometry module to determine the changes in the sensor's current and measure the sensitivity of our sensor when it is exposed to different target gases at room temperature.

Chapter 4: Results and Discussion

4-1. Material Characterizations

4-1-1. X-ray Diffraction Patterns

The comparison of the XRD pattern of ZAD, which had been heated at 580°C for different time spans, including 1 hour, 3 hours, 7 hours, 12 hours, and 21 hours, with the standard pattern of a hexagonal wurtzite structure of polycrystalline ZnO (reference JCPDS Card, No. 96-230-0131) can be seen in Figure 4-1. The results show that the ZnO structures were generated when the material was subjected to 580 ºC for more than 1h. Based on the analyzed data using the HighScore Plus software, it was determined that the 12-hour heating period resulted in a sample closest to the standard polycrystalline ZnO structure. In the XRD pattern, 12 characteristic peaks can be observed at 2theta values of 31.8, 34.4, 36.3, 47.6, 56.6, 62.9, 66.4, 68.0, 69.1, 72.6, 77.0, and 89.6, corresponding to (100), (002), (101), (102), (110), (103), (200), (112), (201), (004), (200), and (210), which are shown in Figure 4-1A. The shift in the ZnO peaks by increasing annealing time can be due to diffusion of different atoms, recrystallization and sintering, and crystal growth and coarsening.

In Figure 4-1b, the XRD results for ZAD heated at different temperatures (280°C, 380°C, 480°C, and 580°C) for 12 hours are presented. It is worth noting that all 12 characteristic peaks corresponding to the hexagonal wurtzite structure of polycrystalline ZnO are present in the XRD pattern when the zinc precursor is heated to more than 280 ºC.

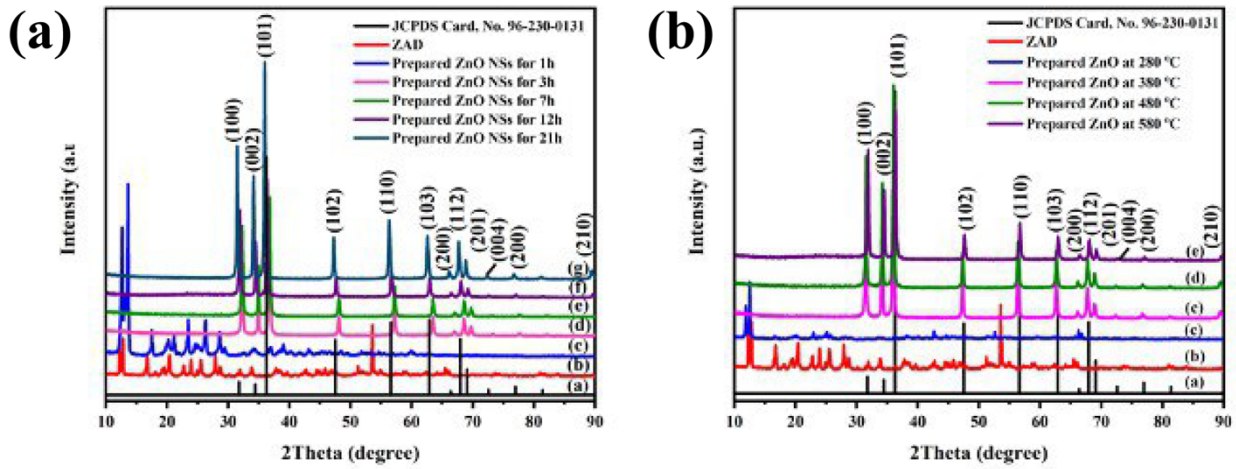

Figure 4-1-a- XRD measurement of ZnO NSs prepared at 580 ºC at different times (0h, 1h, 3h, 7h, 12h, 21h), and b- different temperatures (280 ºC, 380 ºC, 480 ºC, 580 ºC), compared with the JCPD card No. 96-230-0131.

Additionally, the sputtered Au NPs on the ZnO NSs prepared at 380°C were also characterized using XRD (Figure 4-2). Two extra peaks are visible at 2*Theta values of 37.7° and 44.1°, corresponding to the (111) and (200) crystallographic planes, which are indicative of the presence of the Au NPs.

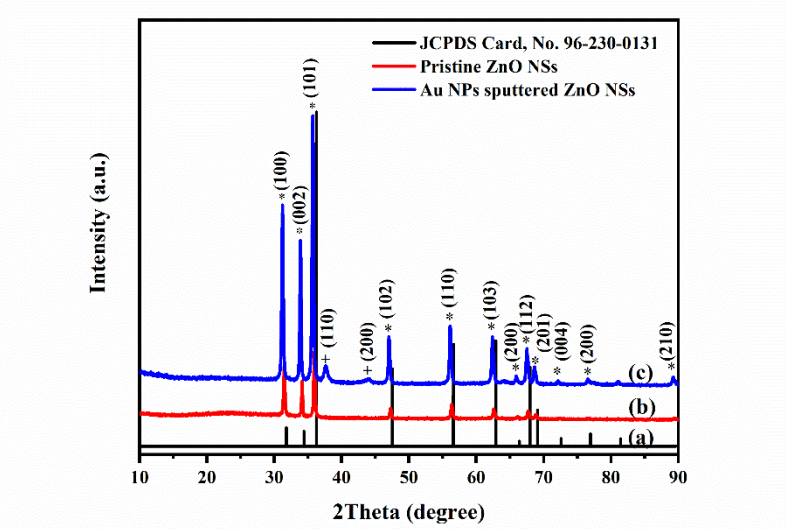

Figure 4-2- XRD measurements of (a) JCPD card No. 96-230-0131, (b) prepared ZnO NSs at 380 ºC for 12h, (c) Au NPs sputtered the same ZnO NSs.

Figure 4-3 shows the intensity in the range of 2theta equal to 37° - 42° with higher resolution, the crystalline size of Au NPs can be calculated by using the Debye-Scherrer formula.

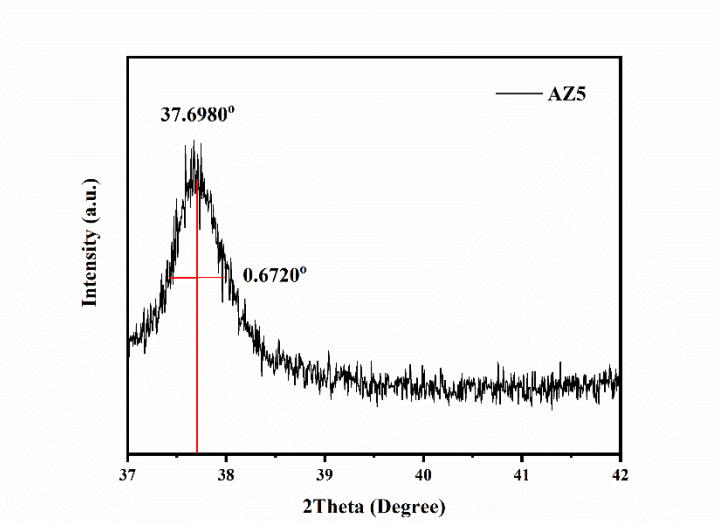

Figure 4-3- High resolution of (111) Au NPs peak in Au NPs sputtered on the ZnO NSs, showing FWHM, and the peak position.

The Debye-Scherrer formula is shown in eq. (1):

$$D_{nm} = \frac{0.9 * \lambda_{nm}}{\beta_{rad} * \cos(\theta_{rad})} \quad (1)$$

where λ is the wavelength of the incident x-ray, which is 1.54 Å, β is the full width at half maximum (FWHM) and $\boldsymbol{\theta}$ is the diffraction angle, which are 0.6720° and 37.6980°, respectively. By applying the values in equation (1), the crystalline size can be calculated, which is around 13.05 nm.

4-1-2. Scanning Electron Microscopy

In Section 2, we demonstrated the fabrication of ZnO NSs through a combination of CBD and TD. The CBD method comprises a two-step process for synthesizing ZnO NSs. In the initial step, as depicted in the SEM micrograph, a seed layer is created (Figure 4-4a). In the next step, ZnO

nanosheets and nanorods are grown in alignment on this seed layer, as shown in Figure 4-4a and Figure 4-4b.

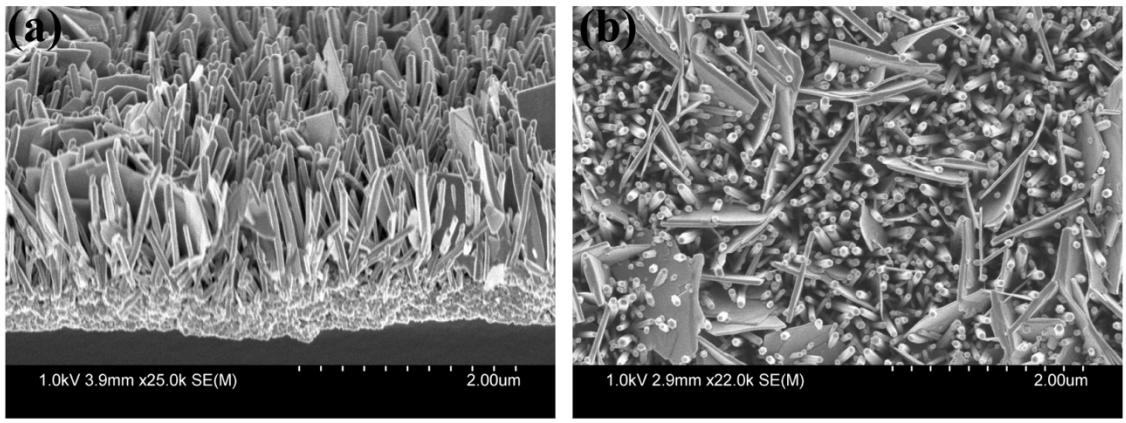

Figure 4-4- SEM image of synthesized ZnO NSs prepared by CBD methods from (a) cross-section (b) top-view.

The morphology of the ZnO NSs prepared using the TD method is composed of unaligned nanorods, shown in Figure 4-5a-c. The size of the nanorods varies since ZnO NSs are fabricated at different temperatures (380 ^{o}C, 480 ^{o}C, and 580 ^{o}C). The length of the developed ZnO nanorods at 580 ^{o}C, 480 ^{o}C, and 380 ^{o}C are 1.48 μm, 345.8 nm, and 280.5 nm, respectively.

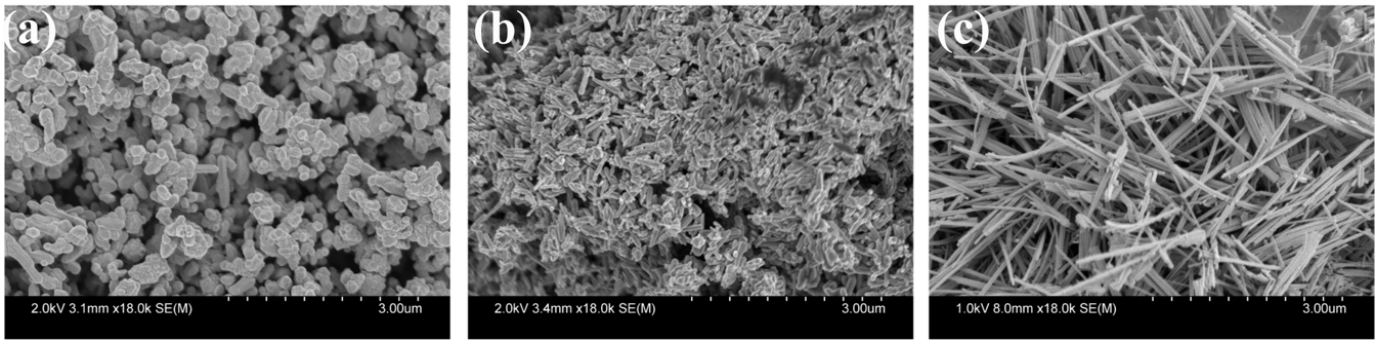

Figure 4-5- SEM image of synthesized ZnO NSs at (a) 380 ^{o}C, (b) 480 ^{o}C, (c) 580 ^{o}C.

4-1-3. Energy Dispersive X-ray spectroscopy (EDS)

To understand the composition and distribution of different elements in the sample, EDS was used. Figure 4-6a-c exhibits the uniformly distributed Zn and O in the sample in ZnO prepared at 380 ºC for 12 h. In this sample, the Zn and O atomic content are 44.25% and 55.74%, respectively. The reason why there are more Zn than O in ZnO structures is the presence of some defects like oxygen vacancies.

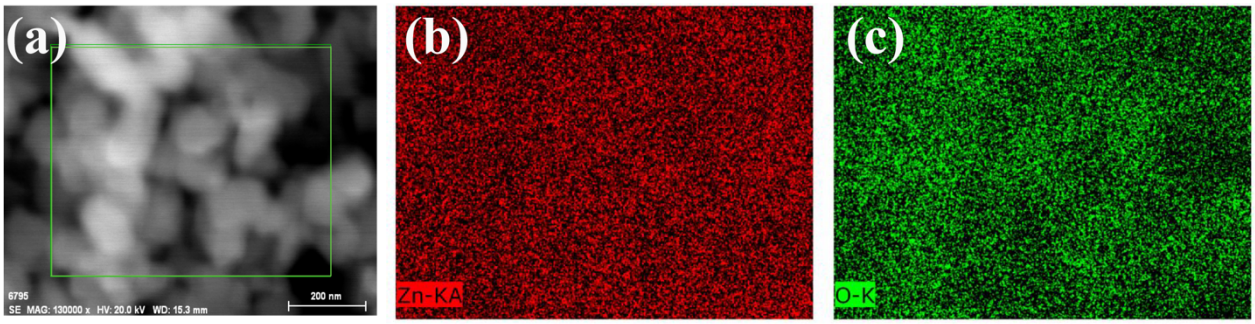

(d)

El	AN	Series	Atom. C [at.%]	Error [%]
O	8	K-series	44.25	2.7
Zn	30	K-series	55.74	2.2
Au	79	M-series	0.01	0.0
		Total:	100.00	

Figure 4-6-a- SEM/EDS image of ZnO prepared at 380 ºC, and the EDS map of b- Zn and c- O, d- available elements, atomic number, type of the produced electron type, atomic percent and error in the atomic percent..

The ZnO NSs, sputtered with 0.1nm-thick Au were characterized by EDS. The result shows that the distribution of Au is uniform in both samples. The atomic percentage of zinc, oxygen, and Au are 45.61%, 53.18%, and 1.21%, respectively (Figure 4-7 a-f). The reason why there is more oxygen than zinc in this structure can be due to the fact that Au has a high affinity toward oxygen on an atomic scale, so it can interact with oxygen in the ambient atmosphere.

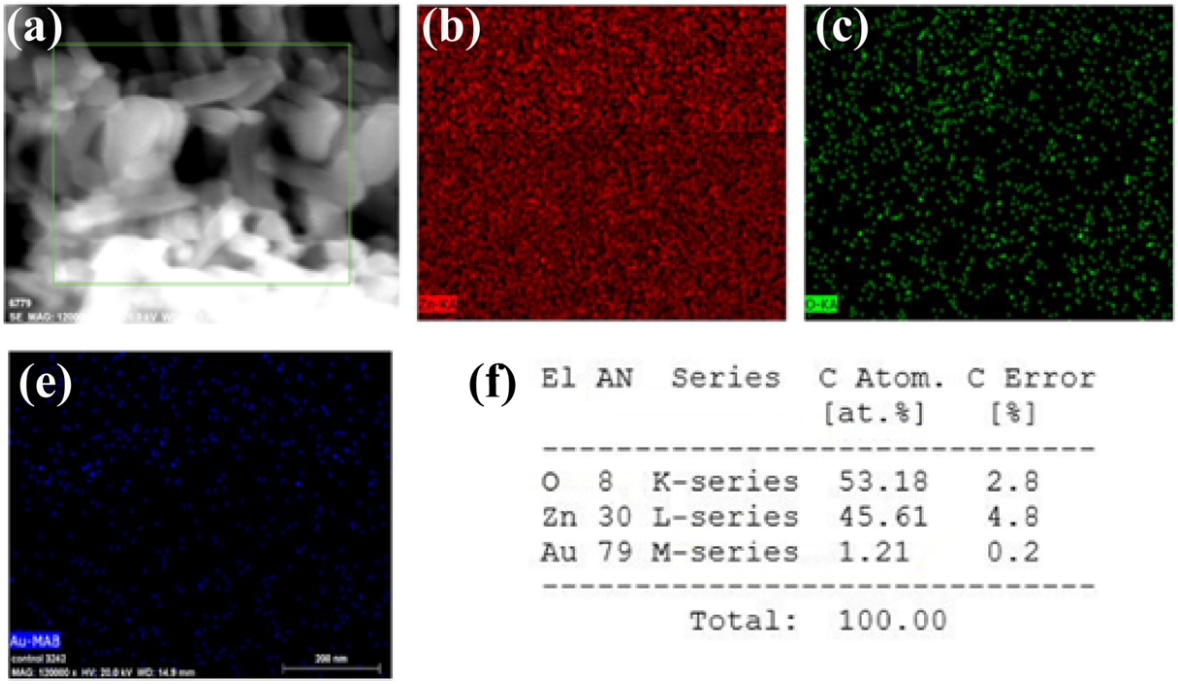

Figure 4-7-a- SEM/EDS image of Au-ZnO NSs prepared at 380 oC, and the EDS map of b- zinc and c- oxygen, d- gold, and e- available elements, atomic number, type of the produced electron type, atomic percent and error in the atomic percent.

4-1-4. X-ray photoelectron spectroscopy (XPS)

XPS was applied to analyze the elemental composition and oxygen vacancy presence in both ZnO NSs and Au-ZnO heterostructures. To ensure accuracy, all binding energy data underwent meticulous calibration using the C1s peak at 284.8 eV. The XPS spectra of ZnO NSs, highlighting distinct peaks corresponding to Zn and O elements in Figure 4-8a. Further insights into the elemental composition emerge in the high-resolution XPS spectra of Zn 2p and O 1s, shown in Figure 4-8b and c, respectively. The peaks at 1021.2 eV and 1044.4 eV in Figure 4-8b are ascribed to Zn 2p3/2 and 2p1/2, respectively, with a spin–orbit splitting energy of 23.2 eV [62], [63]. Additionally, the peak at a binding energy of approximately 530.4 eV is identified as the O 1s spectrum of ZnO NSs. To explore the oxygen states more profoundly, the O1s peak is deconvoluted into two distinct peaks at 531.7 eV and 530.1 eV, corresponding to O_{Def} (oxygen vacancies) and O_{Lat} (lattice oxygen), respectively (Figure 4-8c). This deconvolution yields

valuable insights into the oxygen environment of the analyzed ZnO NSs [64], [65]. Notably, the proportion of O_{Def} among the available oxygen species in this sample is determined to be 25.63%.

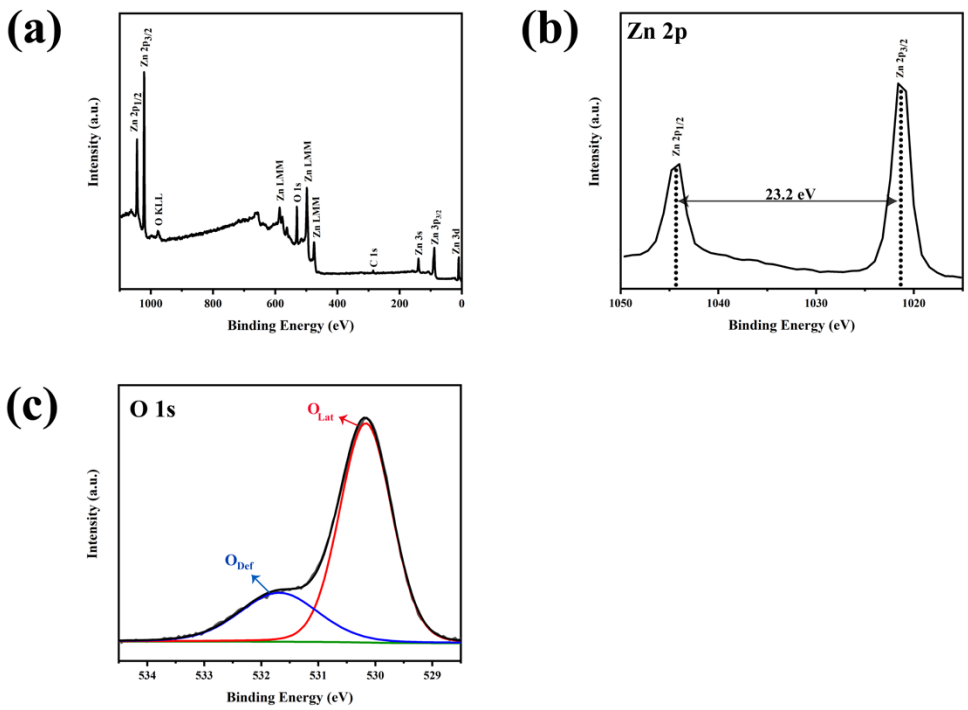

Figure 4-8-a Overview XPS of pure ZnO, and high-resolution XPS spectra of b- Zn 2p, and c- O 1s in pure ZnO sample.

Figure 4-9 presents the XPS analysis of ZnO NSs sputtered with Au NPs. The comprehensive spectra of Au-ZnO heterostructures unveil distinct peaks representing Zn, O, and Au elements (Figure 4-9a). Similar to the characteristics observed in pristine ZnO NSs, the peaks at 1021.6 eV and 1044.8 eV in Figure 4-9b are attributable to Zn 2p3/2 and 2p1/2, respectively. The O 1s peak at around 532 eV, as depicted in Figure 4-9c, exhibits a deconvolution pattern compared to pure ZnO NSs. Instead of the two deconvoluted peaks at 532.1 eV and 531.1 eV associated with O_{Def} and O_{Lat}, an additional peak at 533.1 eV emerges, corresponding to O_{Loo} (loosely bound oxygen). This peak suggests the presence of chemisorbed or dissociated oxygen, or OH species on the surface of Au-ZnO heterostructures. The results underscore a disparity in the percentage of O_{Def}

between pure ZnO and Au-ZnO samples. Specifically, the O_{Def} percentage in pure ZnO is 25.63%, whereas a comparable amount in the Au-ZnO sample is 5.94%. This finding aligns with EDS analysis, indicating that the higher affinity of oxygen towards Au leads to a decrease in the O_{Def} portion. Finally, Figure 4-9d illustrates the detailed high-resolution spectra of Au 4f. Following the deconvolution of the Au 4f peak, three distinct peaks appear at 89.1 eV, 87.9 eV, and 84.2 eV, corresponding to Au 4p7/2, Au 4p 5p, and Zn 3p3/2, respectively.

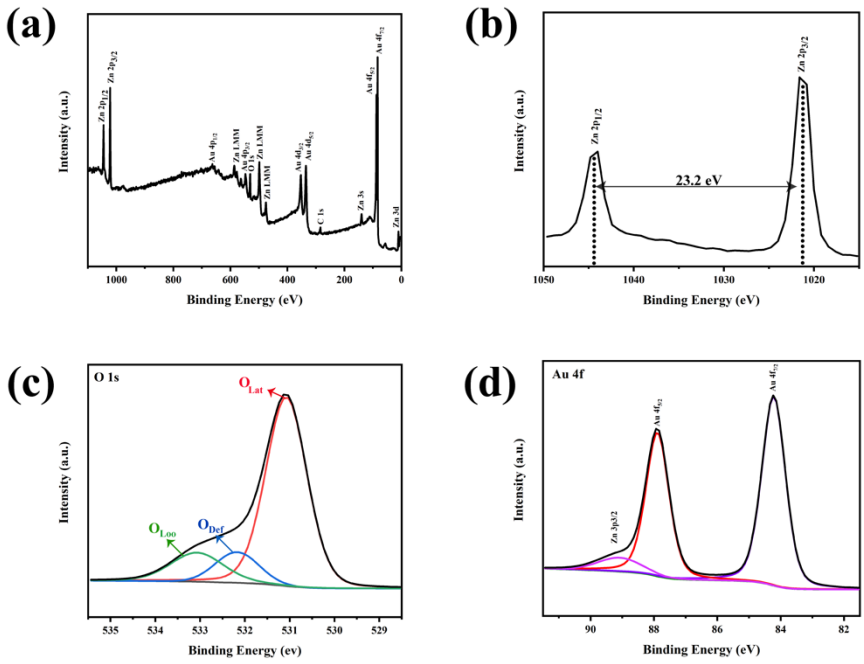

Figure 4-9-a Overview XPS of Au-ZnO heterojunction, and high-resolution XPS spectra of b- Zn 2p, and c- O 1s, d- Au 4f in the Au-ZnO heterostructures.

Following sputtering with Au NPs, Figure 4-10a,b illustrates alterations in bonding energy observed in the O 1s and Zn 2p peaks. The creation of Au-ZnO heterostructures induces a transformation in charge carriers between the Au NPs and the ZnO structure. This occurrence results in modifications to the electrical properties, directly impacting the observed shift in XPS peaks. Specifically, the change in bonding energy for both Zn 2p1/2 and Zn 2p3/2 is 0.4 eV, while the change for O_{Lat} is 1.0 eV. This shift is attributed to a change in the electrical structure of Zn

and O due to the interaction between Au NPs and ZnO NSs. The alteration in the electrical structure is linked to the charge transfer between ZnO NSs and Au NPs.

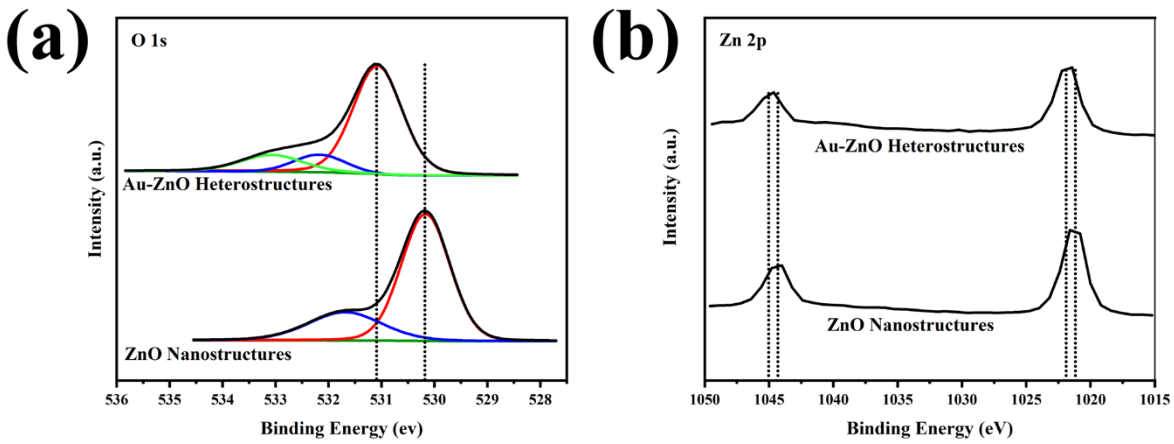

Figure 4-10- The high-resolution spectra of a- O 1s and b-Zn 2p of ZnO NSs and Au-ZnO heterostructures.

4-2. Sensing Characterization

4-2-1. Sensing Response of Bare ZnO Sensor

The best ZnO nanosheets (ZnO NSs) to use as a sensing material were evaluated after the gas sensing setup had been established. We specifically compared the sensing capabilities of ZnO NSs produced at 380 °C, 480 °C, and 580 °C when subjected to various humidity levels, shown in Figure 4-11. The ZnO-based sensor designed at 380 °C was found to have the best response to humidity. This result can be attributed to the fact that some defects, like oxygen vacancies, are more likely to form at lower temperatures. The performance of the sensor is improved by these flaws acting as active sites that easily interact with the target gas.

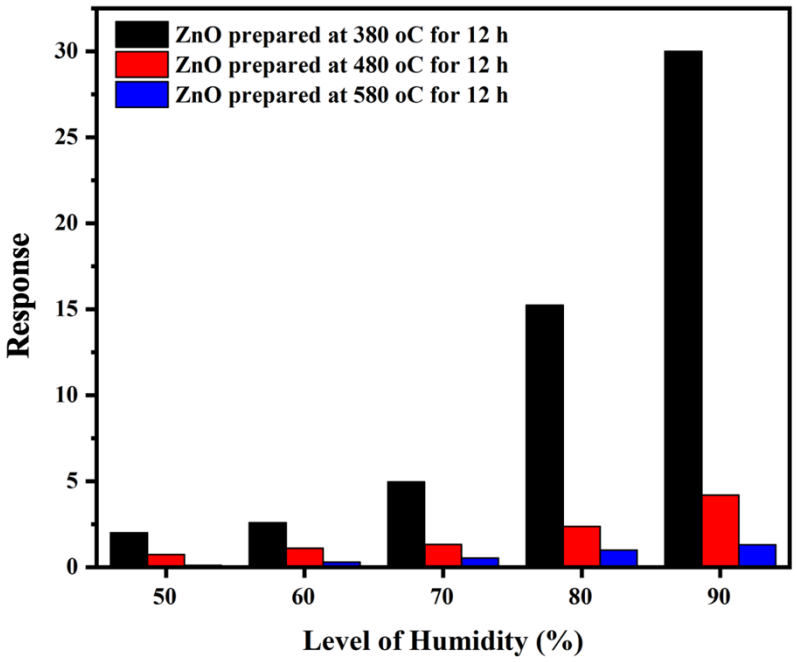

Figure 4-11- Response ZnO-based sensing materials, prepared at a- 380 ºC, b-480 ºC, and c-580 ºC for 12 h toward RH=70%.

In this extensive study, we explored the complex dynamics of a sensor's reaction to exposure to a specific concentration of a target gas within a predetermined humidity range. Our method of investigation consists of a meticulous two-step procedure that aims to explain how the sensor behaves in these circumstances. Through this work, we gain fundamental comprehension of the sensor's default behaviour under a range of humidity levels, which serves as an essential benchmark.

The sensor's current response in the presence of only humidity is represented by the symbol I_{RH} and the sensor's current response in the presence of both target gas as well as humidity is represented by the symbol I_{RH+gas}. This measurement captures the sensor's response to how the target gas interacts with sensing materials at particular humidity conditions. The combination of these two crucial values, I_{RH} and I_{RH+gas}, represents the pivotal point in our research. Applying a mathematically equation, denoted as Eq. 2, one can determine the sensor's response to the target

gas within the specified humidity parameters. This equation is essential for calculating the sensor's sensitivity and reactivity to the target gas under controlled humidity levels, which in turn greatly advances our comprehension of how well the sensor will perform in practical settings.

$$R = \frac{|I_{RH} - I_{RH+Gas}|}{I_{RH}} \quad (2)$$

4-2-2. Sensing Response of Au-ZnO Sensor

To measure the efficiency of the fabricated sensor, different thicknesses of Au nanoparticles were sputtered onto the gas sensor. The ZnO-based gas sensor was sputtered with 0.05 nm, 0.1 nm, 1 nm, 5 nm, and 10 nm-thick Au nanoparticles. Figure 4-12 shows the sensor response for 2000 ppm of ethanol within a humidity range of 50% - 90% RH. The results in Figure 4-12 show that the response of the sensor varies based on the humidity in the absence or minimal presence of Au nanoparticles (> 0.05 nm). Conversely, when the thickness of the gold layer reaches 5 nm or 10 nm, a notable reduction in sensor response is observed (Figure 4-12). This decrease in sensitivity can be attributed to the formation of a barrier layer on the sensing materials, which hinders the effective interaction between the target gas and the sensor's sensing materials. Consequently, the sensor's signal becomes significantly attenuated, making it challenging to detect and measure with precision. As a result, there are two thickness (0.1 nm and 1 nm) of material that are optimal in terms of possessing a relatively stable response toward 2000 ppm ethanol at different levels of humidity. Among these two sensors, the sensor sputtered with 0.1 nm Au NPs is the most promising option, as not only does it experience a roughly stable response at different humidity levels, but the response of this sensor is higher than that of the 1-nm thick Au-ZnO sensor. The reported thickness of Au NPs is not a true representation of their actual thickness; rather, it reflects the measurement provided by the instrument. Consequently, the observed thickness may appear lower than the crystalline size of the Au NPs, which is measured at 13.05 nm. The formation of

clustered Au NPs after sputtering can be attributed to factors such as agglomeration during the sputtering process, as well as the limited mobility and diffusion of atoms onto the substrate surface. So. the 13.05 nm is correlated to the crystalline size of Au NPs in these clustered areas.

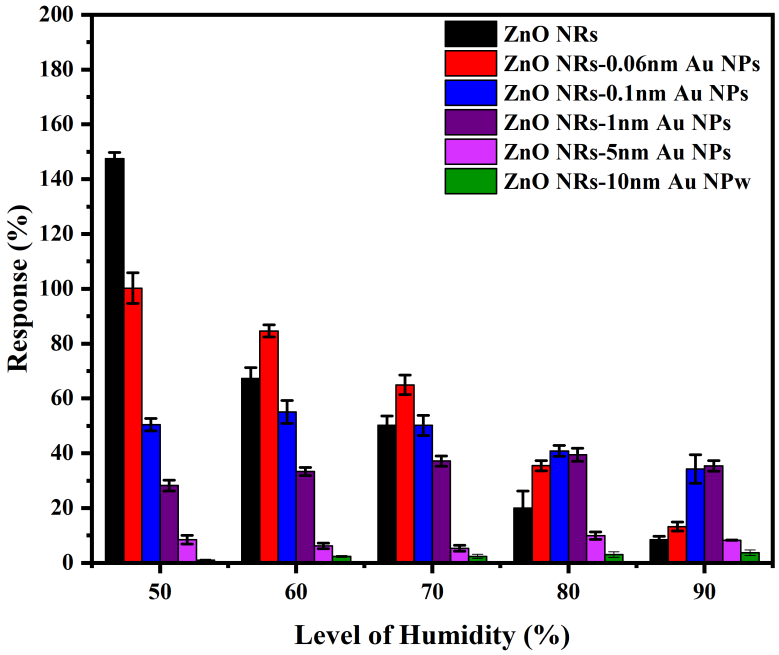

Figure 4-12- Response of ZnO sensor, and ZnO-based sensor, sputtered with different thicknesses of Au NPs (0.05 nm, 0.1 nm, 1 nm, 5 nm, 10 nm) toward 2000 ppm of ethanol at various levels of humidity.

Based on the experimental results in Figure 4-12, the AZ2 is the most effective sample in mitigating humidity impacts for sensing ethanol. Apart from ethanol sensing, AZ2 reveals a reliable response when exposed to 2000 ppm of TEA at different humidity levels (Figure 4-13).

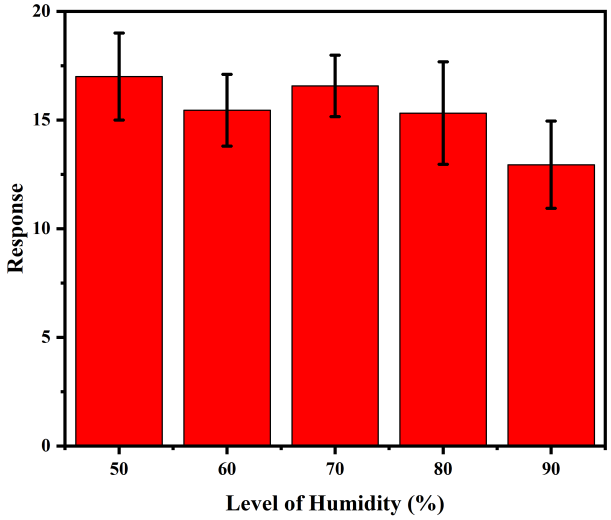

Figure 4-13-Response of AZ2 toward 2000 ppm TEA at different RH.

4-2-3. Selectivity Toward TEA at RH=%70

Selectivity is important for applications involving gas sensing. The 0.1 nm Au sputtered ZnO sensor demonstrates an exceptionally high degree of selectivity towards TEA, with a response of 17.57 which is higher than Acetone, Methanol, Diethyleneamine, Benzene, Toluene, Ethanol, 1-propanol, and H_2 with a response of 0.28, 0.29, 3.65, 2.12, 4.08, 0.41, 0.25 and 0.06, respectively. The response of the sensor to other target gases at a relative humidity of 70% and a concentration of 2000 ppm is lower than that of TEA (Figure 4-14).

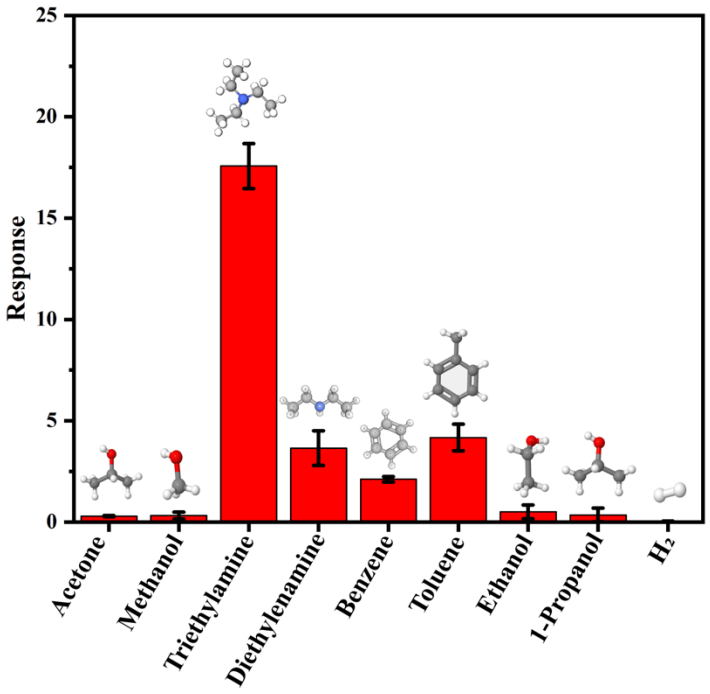

Figure 4-14- Response of 0.1 nm-sputtered Au onto the ZnO sensor to different gases at 2000 ppm and RH=70%.

Au-ZnO sensors improved gas sensing properties can be explained by two main mechanisms: Schottky barrier effects that result from the heterostructure formation and catalytic effects that are made possible by the presence of Au nanoparticles. Electron transfer from ZnO semiconductors to Au nanoparticles is facilitated by the unique band structure of the Au-ZnO heterostructure and the electric field generated. By transferring electrons, the structure becomes more conductive overall, which makes it easier to separate charge carriers like electrons and holes and lowers the rate at which they recombine. The O^{2-} ions are produced at room temperature when more oxygen molecules interact with the electrons created by the structure's increased electron generation. A wider depletion layer is the outcome of this process, as Figure 4-15a and b illustrate. These created oxygen ions then interact with the TEA gas target to produce more electrons, which increases conductivity and decreases resistance even more. As Figure 4-15c shows, this electron inflow also

contributes to a decrease in the depletion layer's width. It's also significant that the absorbed humidity molecules on the sensor experience a catalytic effect due to the presence of Au nanoparticles. The dissociation of humidity molecules into OH- and H+ ions is the result of this catalytic influence.

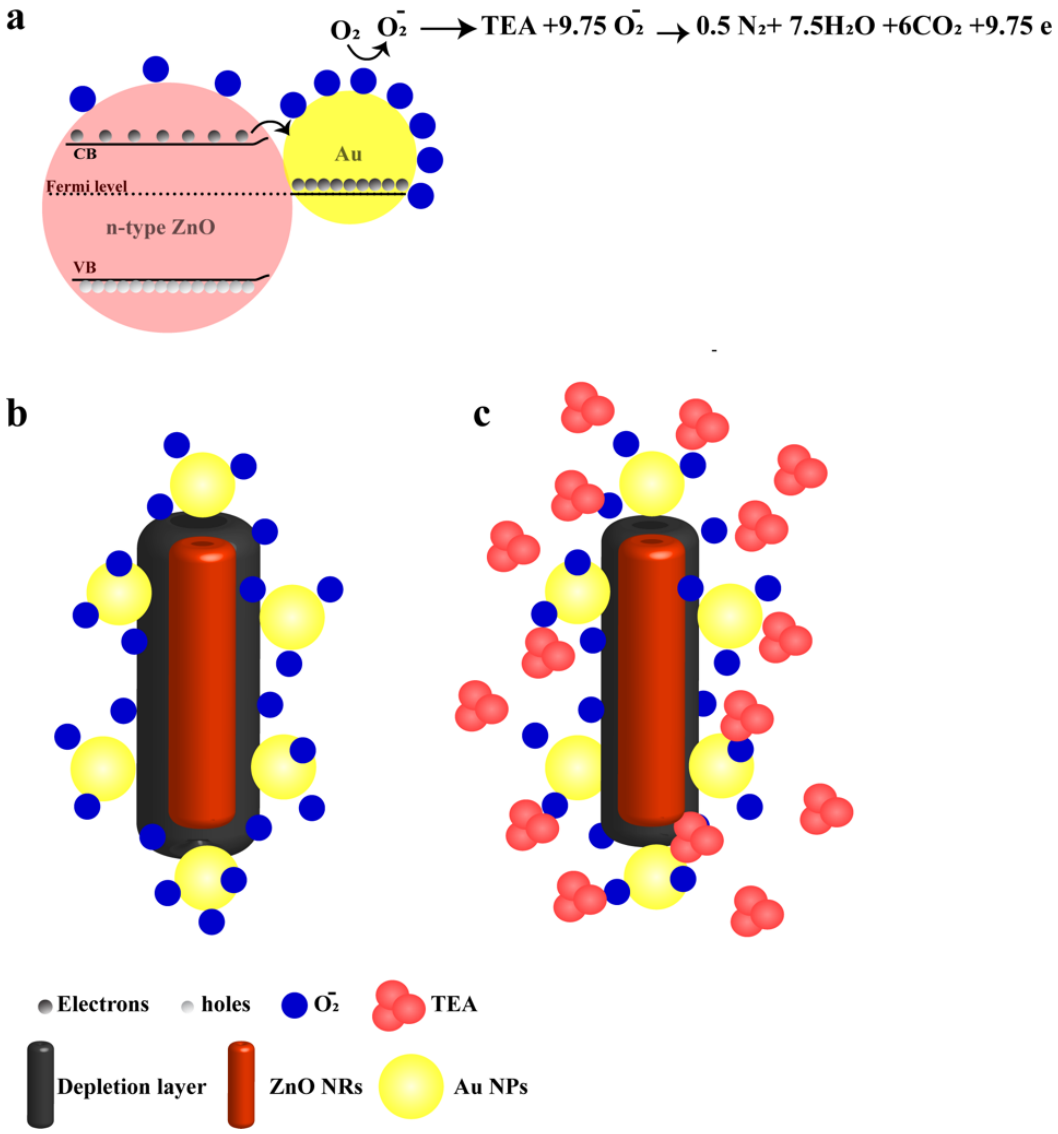

Figure 4-15-a- Au-ZnO heterojunction band gap structure, b- Au-ZnO sensing materials in the air atmosphere without and c- with TEA.

The primary basis for the underlying sensing mechanism is a chemical interaction. It happens when different target gases mix in the atmosphere and interact with room-temperature oxygen ions

adsorbed on the sensor's surface. Electrons from the conductive band of the sensing materials have an attraction for the oxygen molecules that adhere to the sensor's surface. Different oxygen ion species are produced as a result of this interaction, and they all form at different temperatures (reactions 1-4) [66]. The reaction between the produced oxygen ions and target gas molecules produces the differentiating sensing response. Different target gases can produce different amounts of electrons, which can lead to variations in conductivity, as reactions 5–13 demonstrate, which correspond to the interaction of oxygen ion with TEA, acetone, methanol, ethanol, toluene, isopropanol, diethylamine, benzene, and hydrogen gas, respectively. In addition to the quantity of generated electrons, the polarity of gas molecules plays a crucial role in this application. Occasionally, a moisture barrier may form between the gas target and the sensing materials, potentially impacting polar molecules. Reactions 5–13 demonstrate that the presence of polar TEA results in a higher electron generation which is aligned with the selectivity study, shown in Figure 4-15 [53], [67]–[74].

$$O_2(g) \rightarrow O_2(ads) \quad (1)$$

$$O_2(g) + e^- \rightarrow O_2^-(ads) \quad (T < 100\ ℃) \quad (2)$$

$$O_2(g) + e^- \rightarrow O^-(ads) \quad (100\ ℃ < T < 300\ ℃) \quad (3)$$

$$O_2(g) + e^- \rightarrow O^{2-}(ads) \quad (T > 300\ ℃) \quad (4)$$

$$N(C_2H_5)_3 + {}^{39}/_4\, O_2^- \rightarrow {}^1/_2\, N_2 + {}^{15}/_2\, H_2O + 6CO_2 + {}^{39}/_4\, e^- \quad (5)$$

$$CH_3COCH_3 + 4O_2^- \rightarrow 3H_2O + 3CO_2 + 4e^- \quad (6)$$

$$CH_3OH + O_2^- \rightarrow HCOOH + H_2O + e^- \quad (7)$$

$$C_2H_5OH + 3O_2^- \rightarrow 2H_2O + 3CO_2 + 3e^- \quad (8)$$

$$C_7H_8 + 9O_2^- \rightarrow 4H_2O + 7CO_2 + 9e^- \quad (9)$$

$$C_3H_8O + {}^9/_2\, O_2^- \rightarrow 4H_2O + 3CO_2 + {}^9/_2\, e^- \quad (10)$$

$$(NH_2CH_2CH_2)_2NH + {}^{29}/_{4}\, O_2^- \rightarrow {}^{3}/_{2}\, N_2 + 6.5H_2O + 4CO_2 + {}^{29}/_{4}\, e^- \quad (11)$$

$$C_6H_6 + {}^{15}/_{2}\, O_2^- \rightarrow 3H_2O + 6CO_2 + 15/2e^- \quad (12)$$

$$H_2 + O_2^- \rightarrow 3H_2O + 6CO_2 + 15/2e^- \quad (13)$$

4-2-4. Stability and Response/Recovery times

The response of the sensor shows promising stability and consistency with minimal fluctuation over 24 days (Figure 4-16a). The response time can be defined as the time that the sensor reaches 90% of the highest current, and the recovery time is the time that the sensor reaches 60% of its ground state. Based on the determination, it is shown that the response and recovery times are 9.8 s and 4.4 s, respectively (Figure 4-16b).

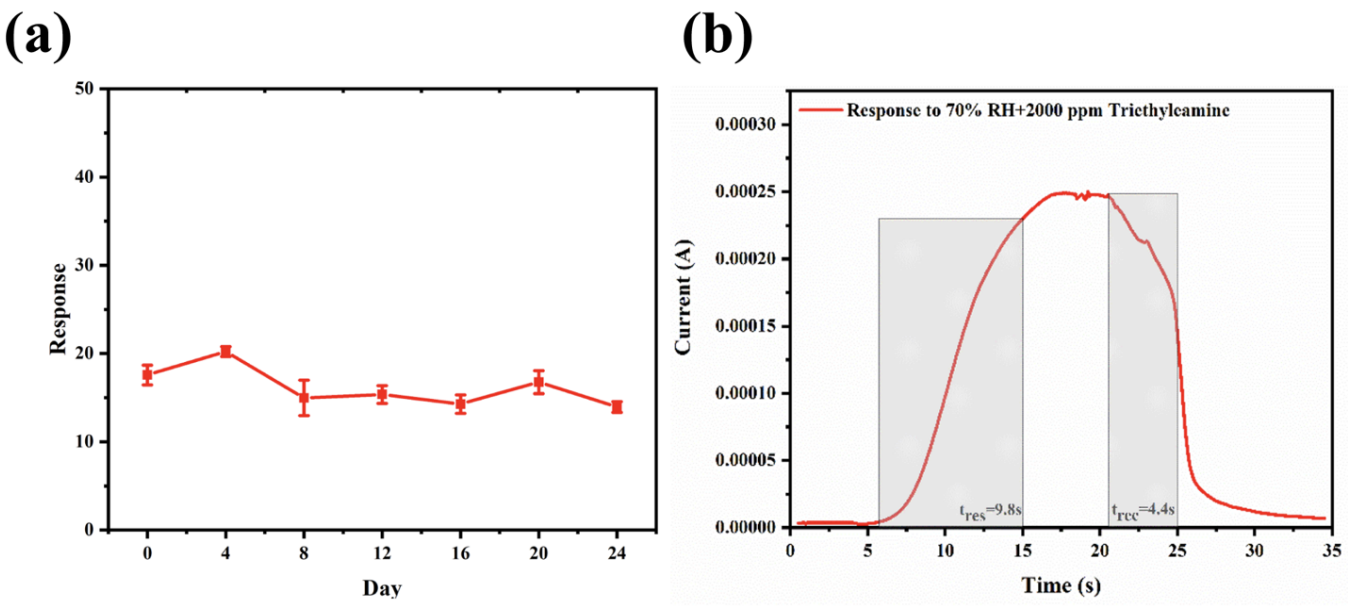

Figure 4-16-a-The sensor response to 2000 ppm TEA at RH=70% over time, b- response/recovery time for AZ2.

4-2-5. Calibration Plot

In order to assess the response of the sensor across a range of concentrations, we selected five distinct concentration levels, including 100 ppm, 250 ppm, 500 ppm, 750 ppm, and 1000 ppm. Figure 4-17 shows the fitted curve which demonstrates a high accuracy of fit ($R^2 \approx 0.94$). Using

this fitted curve, we can extrapolate to estimate the sensor's response at concentrations beyond this concentration range.

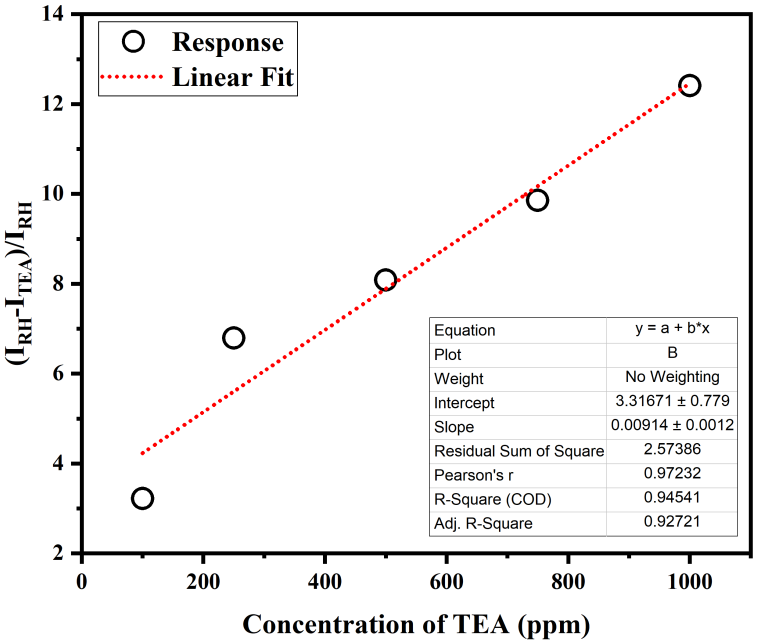

Figure 4-17- Calibration curve for the response of the sensor at different concentrations.

To compare this research work with previous research on TEA detection at different temperatures and concentrations, Table 4-1 is provided. It's crucial to remember that because of variations in the research approaches and response calculation formulas utilized in these studies, the response values may not be directly comparable. Our research is primarily focused on using Au catalysts to address the problem of humidity interference. As a result, our method includes subtracting the sensor's response to TEA at a given humidity level from the sensor's response at that same humidity level Section 4-2-1. It is noteworthy to emphasize that our research's operating temperature is notably lower than the temperatures employed in the studies shown in Table 4-1.

Table 4- 1- Comparison of different parameters in ZnO-based sensor for the detection of TEA.

	Sensing Materials	Temp. (°C)	Response	Res/Rec time (s)	Ref.
1	CuO/ZnO P-N heterostructural nanorods	40	8@50 ppm	5-25	[75]
2	Au-Loaded ZnO/SnO_2 Core− Shell Nanorods	40	12.4@50 ppm	1.24-long time	[76]
3	ZnS@ZnO core-shell	200	74.65@100 ppm	3-176	[77]
4	CuO@In_2O_3/ZnO Core−ShellNanorods	RT	25@10 ppm	246-long time	[78]
5	Au–ZnO nanoflower	200	276@10 ppm	---	[79]
6	hierarchical radial CeO_2/ZnO n-n heterojunction	200	92.17@100 ppm	29-23	[80]
7	BiOBr Micro flowers Decorated with ZnO Nanocrystals	200	20.57@100 ppm	4-N/A	[28]
8	Anchoring Pt Particles onto Mesoporousized ZnO	200	535@200 ppm	8.49-3.2	[81]
9	ZnO/MoO_3 heterostructures	180	519@100 ppm	9-16	[82]
10	Pr-doped ZnO nanospindles	200	158@50 ppm	10-46	[83]
11	Sputtered Au NPs-ZnO NSs	25	17.57@2000 ppm	9.8-4.4	This work

Chapter 5- Conclusion

5-1. Summary

The study involved comprehensive material characterizations and sensing characterizations of ZnO NSs with a focus on gas-sensing applications. ZnO NSs were prepared using both CBD and TD methods, but because of its simplicity, the TD method was selected as the main preparation method for material development. Key findings and observations are as follows:

XRD patterns of ZnO NSs heated at different temperatures and times revealed that ZnO structures are formed when subjected to 380 °C for more than 3 h. The ZnO nanosheets heated for 12 h at different temperatures closely resemble the standard polycrystalline ZnO structure, showing 12 characteristic peaks indicative of a hexagonal wurtzite structure. SEM images depicted the formation of seed layers in the initial step and the growth of aligned ZnO nanorods on these seed layers in subsequent steps. The morphology of ZnO NSs prepared by the TD method showed unaligned nanorods of varying lengths depending on the fabrication temperature. EDS was used to determine the composition and distribution of elements. The ZnO prepared at 380°C contained uniformly distributed Zn and O, with less oxygen than zinc due to the presence of defects like oxygen vacancies. ZnO nanorods sputtered with Au NPs showed uniform distribution of Au, Zn, and O, with the excess oxygen attributed to Au's high affinity for oxygen on an atomic scale. The study evaluated the gas sensing capabilities of ZnO NSs fabricated at different temperatures (380 °C, 480 °C, and 580 °C) in response to various humidity levels. ZnO NSs produced at 380°C exhibited the best response to humidity, potentially due to the formation of defects like oxygen vacancies at lower temperatures, which enhanced the sensor's performance. The results showed that the ZnO sputtered with 0.1 nm-thick Au NPs revealed a stable response toward 2000 ppm of ethanol and TEA at various levels of humidity. The 0.1 nm-thick Au nanoparticles sputtered onto ZnO sensor exhibited high selectivity to TEA, with a response of 17.57 which is 62.75, 60.59,

4.81, 8.29, 4.30, 42.85, 70.28, and 292.83 times higher than the response toward Acetone, Methanol, Diethyleneamine, Benzene, Toluene, Ethanol, 1-propanol, and H_2 at a 70% relative humidity and a concentration of 2000 ppm, respectively. The sensor displayed excellent stability over 24 days with minimal fluctuations. The response and recovery times were measured at 9.8 seconds and 4.4 seconds, respectively, indicating a rapid and reliable sensing performance. The study included an assessment of the sensor's response across a range of TEA concentrations from 100 ppm to 1000 ppm, demonstrating a high degree of accuracy in concentration-response estimation. The material characterizations revealed the structural properties of ZnO nanosheets, while the sensing characterizations demonstrated the high sensor response and selectivity, along with stability and recovery times for practical gas sensing applications.

5-2. Contribution

The study has made several significant contributions:

- Synthesized ZnO nanostructures with sputtered Au NPs that were characterized with various techniques.
- Utilized Au NPs to address the adverse effects of humidity on ZnO-based gas sensors and optimized the best thickness of sputtered Au NPs
- Conducted characterization measurements to better understand the ZnO NSs, including understanding the morphology, size, element distribution, chemical composition, and other properties of the synthesized materials.
- Fabricated a gas sensing setup to change the humidity levels and evaluate the performance of the Au NPs-ZnO NSs sensor for TEA detection at room temperature.
- Employed a chemiresistive sensor to determine the change in resistance and calculate the response toward different target gases.

- Created a calibration plot to evaluate the response to TEA using concentrations beyond the range of analysis by extrapolating the fitted curve.

5-3. Future Work

While this thesis has focused on the development of a proof-of-concept sensor based on ZnO NSs sputtered with Au NPs to mitigate the detrimental impacts of humidity on gas measurements, there are still lots of gaps. Improvements can be made to enhance the efficiency of the fabricated sensor as follows:

- Use other catalysts: Au NPs are among the most used catalysts, employed in different research fields and applications; however, they suffer from being expensive and less accessible. So, it is recommended to work with other cheaper catalysts like carbon (C), copper (Cu), iron (Fe), magnesium (Mn), etc.
- Sensitivity improvements: Several methods can be used to improve the effectiveness of the performance of the sensor. One of these methods is using ultraviolet (UV) light to produce more charge carriers and increase the number of absorbed oxygen ions to react with gas targets and improve the efficiency of the fabricated sensor.
- Selectivity Enhancement: This research demonstrates a heightened sensor response specifically to TEA compared to other target gases. To further advance this field, it is suggested that future studies focus on assessing the selectivity of TEA within diverse environmental contexts, considering potential interactions with mixture of various gases.
- Design a more suitable chamber: To achieve greater response accuracy, it is advisable to construct a larger chamber capable of generating lower concentrations of target gases. Additionally, the implementation of programming can offer enhanced control over the duration during which our sensor is exposed to target gases and when exposure is halted.

In conclusion, to enhance the performance of gas sensors, considering cost-effective catalysts like carbon, copper, iron, and magnesium as alternatives to expensive Au nanoparticles is recommended. Sensitivity improvements can be achieved through the application of UV light, which generates more charge carriers and enhances oxygen molecule absorption for better gas target reactions. Additionally, to increase response accuracy, the design of a larger chamber for lower gas concentration generation, along with the utilization of precise programming for exposure control, is advisable. These strategies collectively contribute to improved gas sensing capabilities.

Bibliography

[1] M. Dadkhah and J.-M. Tulliani, "Green synthesis of metal oxides semiconductors for gas sensing applications," *Sensors*, vol. 22, no. 13, p. 4669, 2022.

[2] K. G. Krishna, S. Parne, N. Pothukanuri, V. Kathirvelu, S. Gandi, and D. Joshi, "Nanostructured metal oxide semiconductor-based gas sensors: A comprehensive review," *Sens Actuators A Phys*, vol. 341, p. 113578, 2022.

[3] S. Gai, B. Wang, X. Wang, R. Zhang, S. Miao, and Y. Wu, "Ultrafast NH3 gas sensor based on phthalocyanine-optimized non-covalent hybrid of carbon nanotubes with pyrrole," *Sens Actuators B Chem*, vol. 357, p. 131352, 2022.

[4] J. Y. Park *et al.*, "Tuning the sensing responses towards room-temperature hypersensitive methanol gas sensor using exfoliated graphene-enhanced ZnO quantum dot nanostructures," *J Hazard Mater*, vol. 438, p. 129412, 2022.

[5] S. Gasso, M. K. Sohal, and A. Mahajan, "MXene modulated SnO2 gas sensor for ultra-responsive room-temperature detection of NO2," *Sens Actuators B Chem*, vol. 357, p. 131427, 2022.

[6] B.-R. Huang, A. Saravanan, D. Kathiravan, T.-Y. Chiang, and W.-L. Yang, "Growth of Graphitic Carbon Nitride-Incorporated ZnO Nanorods on Silicon Pyramidal Substrates for Enhanced Hydrogen Sensing Applications," *ACS Appl Mater Interfaces*, vol. 14, no. 36, pp. 41481–41488, 2022.

[7] S. Yang *et al.*, "In situ synthesis of MoS2-decorated Zn-doped MoO3 for outstanding hydrogen sensing at room temperature," *Sens Actuators B Chem*, vol. 367, p. 132026, 2022.

[8] Y. Kang, F. Yu, L. Zhang, W. Wang, L. Chen, and Y. Li, "Review of ZnO-based nanomaterials in gas sensors," *Solid State Ion*, vol. 360, p. 115544, 2021.

[9] Ü. Özgür *et al.*, "A comprehensive review of ZnO materials and devices," *J Appl Phys*, vol. 98, no. 4, 2005.

[10] T. Zhou and T. Zhang, "Recent progress of nanostructured sensing materials from 0D to 3D: overview of structure–property-application relationship for gas sensors," *Small Methods*, vol. 5, no. 9, p. 2100515, 2021.

[11] A. K. Pathak *et al.*, "Recent Advances in Sensing Materials Targeting Clinical Volatile Organic Compound (VOC) Biomarkers: A Review," *Biosensors (Basel)*, vol. 13, no. 1, p. 114, 2023.

[12] Y. Jo, Y. K. Jo, J. Lee, H. W. Jang, I. Hwang, and D. J. Yoo, "MOF-based chemiresistive gas sensors: toward new functionalities," *Advanced Materials*, p. 2206842, 2022.

[13] D. Zappa, V. Galstyan, N. Kaur, H. M. M. M. Arachchige, O. Sisman, and E. Comini, "'Metal oxide-based heterostructures for gas sensors'-A review," *Anal Chim Acta*, vol. 1039, pp. 1–23, 2018.

[14] C. Imawan, H. Steffes, F. Solzbacher, and E. Obermeier, "Structural and gas-sensing properties of V2O5–MoO3 thin films for H2 detection," *Sens Actuators B Chem*, vol. 77, no. 1–2, pp. 346–351, 2001.

[15] S. R. Sriram *et al.*, "Nanostructured WO3 based gas sensors: a short review," *Sensor Review*, vol. 41, no. 4, pp. 406–424, 2021.

[16] H. J. Sharma, N. D. Sonwane, and S. B. Kondawar, "Electrospun SnO2/polyaniline composite nanofibers based low temperature hydrogen gas sensor," *Fibers and Polymers*, vol. 16, no. 7, pp. 1527–1532, 2015.

[17] A. N. Abdullah *et al.*, "Correction model for metal oxide sensor drift caused by ambient temperature and humidity," *Sensors*, vol. 22, no. 9, p. 3301, 2022.
[18] H. Kim, A. Haensch, I. Kim, N. Barsan, U. Weimar, and J. Lee, "The role of NiO doping in reducing the impact of humidity on the performance of SnO2-Based gas sensors: synthesis strategies, and phenomenological and spectroscopic studies," *Adv Funct Mater*, vol. 21, no. 23, pp. 4456–4463, 2011.
[19] K. Suematsu, M. Sasaki, N. Ma, M. Yuasa, and K. Shimanoe, "Antimony-doped tin dioxide gas sensors exhibiting high stability in the sensitivity to humidity changes," *ACS Sens*, vol. 1, no. 7, pp. 913–920, 2016.
[20] M. Shooshtari, A. Salehi, and S. Vollebregt, "Effect of humidity on gas sensing performance of carbon nanotube gas sensors operated at room temperature," *IEEE Sens J*, vol. 21, no. 5, pp. 5763–5770, 2020.
[21] A. N. Abdullah, K. Kamarudin, S. M. Mamduh, A. H. Adom, and Z. H. M. Juffry, "Effect of environmental temperature and humidity on different metal oxide gas sensors at various gas concentration levels," in *IOP Conference Series: Materials Science and Engineering*, IOP Publishing, 2020, p. 012152.
[22] J. Wang, S. Fan, Y. Xia, C. Yang, and S. Komarneni, "Room-temperature gas sensors based on ZnO nanorod/Au hybrids: Visible-light-modulated dual selectivity to NO2 and NH3," *J Hazard Mater*, vol. 381, p. 120919, 2020.
[23] Y. K. Moon, S.-Y. Jeong, Y. C. Kang, and J.-H. Lee, "Metal oxide gas sensors with Au nanocluster catalytic overlayer: toward tuning gas selectivity and response using a novel bilayer sensor design," *ACS Appl Mater Interfaces*, vol. 11, no. 35, pp. 32169–32177, 2019.
[24] T. Ueda, N. Oide, K. Kamada, T. Hyodo, and Y. Shimizu, "Improved toluene response of mixed-potential type YSZ-based gas sensors using CeO2-added Au electrodes," *ECS Sensors Plus*, vol. 1, no. 1, p. 013604, 2022.
[25] Y. K. Moon, S.-Y. Jeong, Y. C. Kang, and J.-H. Lee, "Metal oxide gas sensors with Au nanocluster catalytic overlayer: toward tuning gas selectivity and response using a novel bilayer sensor design," *ACS Appl Mater Interfaces*, vol. 11, no. 35, pp. 32169–32177, 2019.
[26] J. Liu, L. Zhang, J. Fan, and J. Yu, "Semiconductor gas sensor for triethylamine detection," *Small*, vol. 18, no. 11, p. 2104984, 2022.
[27] J. Liu, L. Zhang, J. Fan, and J. Yu, "Semiconductor gas sensor for triethylamine detection," *Small*, vol. 18, no. 11, p. 2104984, 2022.
[28] X. Xu *et al.*, "Triethylamine Gas Sensors Based on BiOBr Microflowers Decorated with ZnO Nanocrystals," *ACS Appl Nano Mater*, vol. 5, no. 10, pp. 15837–15846, 2022.
[29] H. Zhang, Y. Guo, and F. Meng, "Metal oxide semiconductor sensors for triethylamine detection: sensing performance and improvements," *Chemosensors*, vol. 10, no. 6, p. 231, 2022.
[30] J. Liu, L. Zhang, J. Fan, B. Zhu, and J. Yu, "Triethylamine gas sensor based on Pt-functionalized hierarchical ZnO microspheres," *Sens Actuators B Chem*, vol. 331, p. 129425, 2021.
[31] J. Liu, L. Zhang, J. Fan, and J. Yu, "Semiconductor gas sensor for triethylamine detection," *Small*, vol. 18, no. 11, p. 2104984, 2022.
[32] M. Poloju, N. Jayababu, E. Manikandan, and M. V. R. Reddy, "Enhancement of the isopropanol gas sensing performance of SnO 2/ZnO core/shell nanocomposites," *J Mater Chem C Mater*, vol. 5, no. 10, pp. 2662–2668, 2017.

[33] S.-C. Wang *et al.*, "NiO nanoparticles-decorated ZnO hierarchical structures for isopropanol gas sensing," *Rare Metals*, pp. 1–12, 2022.
[34] Q. Zeng, Y. Cui, L. Zhu, and Y. Yao, "Increasing oxygen vacancies at room temperature in SnO2 for enhancing ethanol gas sensing," *Mater Sci Semicond Process*, vol. 111, p. 104962, 2020.
[35] H. Farahani, R. Wagiran, and M. N. Hamidon, "Humidity sensors principle, mechanism, and fabrication technologies: a comprehensive review," *Sensors*, vol. 14, no. 5, pp. 7881–7939, 2014.
[36] D. Zhang, Y. Sun, P. Li, and Y. Zhang, "Facile fabrication of MoS2-modified SnO2 hybrid nanocomposite for ultrasensitive humidity sensing," *ACS Appl Mater Interfaces*, vol. 8, no. 22, pp. 14142–14149, 2016.
[37] Y. Wang and Y. Zhou, "Recent progress on anti-humidity strategies of chemiresistive gas sensors," *Materials*, vol. 15, no. 24, p. 8728, 2022.
[38] M. Weber *et al.*, "High-performance nanowire hydrogen sensors by exploiting the synergistic effect of Pd nanoparticles and metal–organic framework membranes," *ACS Appl Mater Interfaces*, vol. 10, no. 40, pp. 34765–34773, 2018.
[39] Y. Liu and Y. Lei, "Pt-CeO2 nanofibers based high-frequency impedancemetric gas sensor for selective CO and C3H8 detection in high-temperature harsh environment," *Sens Actuators B Chem*, vol. 188, pp. 1141–1147, 2013.
[40] M. Yamaguchi, S. A. Anggraini, Y. Fujio, M. Breedon, V. V Plashnitsa, and N. Miura, "Selective hydrogen detection at high temperature by using yttria-stabilized zirconia-based sensor with coupled metal-oxide-based sensing electrodes," *Electrochim Acta*, vol. 76, pp. 152–158, 2012.
[41] X. Chen, J. Hu, P. Chen, M. Yin, F. Meng, and Y. Zhang, "UV-light-assisted NO2 gas sensor based on WS2/PbS heterostructures with full recoverability and reliable anti-humidity ability," *Sens Actuators B Chem*, vol. 339, p. 129902, 2021.
[42] X. Chen, J. Hu, P. Chen, M. Yin, F. Meng, and Y. Zhang, "UV-light-assisted NO2 gas sensor based on WS2/PbS heterostructures with full recoverability and reliable anti-humidity ability," *Sens Actuators B Chem*, vol. 339, p. 129902, 2021.
[43] J. Wu *et al.*, "Three-dimensional graphene hydrogel decorated with SnO2 for high-performance NO2 sensing with enhanced immunity to humidity," *ACS Appl Mater Interfaces*, vol. 12, no. 2, pp. 2634–2643, 2020.
[44] M. Qin, P. Hou, Z. Wu, and J. Wang, "Precise humidity control materials for autonomous regulation of indoor moisture," *Build Environ*, vol. 169, p. 106581, 2020.
[45] B. Mumyakmaz, A. Özmen, M. A. Ebeoğlu, C. Taşaltın, and İ. Gürol, "A study on the development of a compensation method for humidity effect in QCM sensor responses," *Sens Actuators B Chem*, vol. 147, no. 1, pp. 277–282, 2010.
[46] M. Yang *et al.*, "Acetone sensors with high stability to humidity changes based on Ru-doped NiO flower-like microspheres," *Sens Actuators B Chem*, vol. 313, p. 127965, 2020.
[47] S. Zhang *et al.*, "An acetone gas sensor based on nanosized Pt-loaded Fe2O3 nanocubes," *Sens Actuators B Chem*, vol. 290, pp. 59–67, 2019.
[48] C. Wang, Y. Li, F. Gong, Y. Zhang, S. Fang, and H. Zhang, "Advances in doped ZnO nanostructures for gas sensor," *The Chemical Record*, vol. 20, no. 12, pp. 1553–1567, 2020.
[49] A. Hannon, W. Seames, and J. Li, "Hybrid carbon nanotubes/gold nanoparticles composites for trace nitric oxide detection over a wide range of humidity," *Sensors*, vol. 22, no. 19, p. 7581, 2022.

[50] W. Liu, Y. Xie, T. Chen, Q. Lu, S. U. Rehman, and L. Zhu, "Rationally designed mesoporous In2O3 nanofibers functionalized Pt catalysts for high-performance acetone gas sensors," *Sens Actuators B Chem*, vol. 298, p. 126871, 2019.
[51] Q. Chen *et al.*, "Enhanced acetone sensor based on Au functionalized In-doped ZnSnO3 nanofibers synthesized by electrospinning method," *J Colloid Interface Sci*, vol. 543, pp. 285–299, 2019.
[52] T. Hyodo, W. Sakata, T. Ueda, and Y. Shimizu, "Effects of surface modification of platinum electrodes with gold on hydrogen-sensing properties of diode-type sensors," *ECS Sensors Plus*, vol. 1, no. 1, p. 013602, 2022.
[53] M. Deshwal and A. Arora, "Enhanced acetone detection using Au doped ZnO thin film sensor," *Journal of Materials Science: Materials in Electronics*, vol. 29, pp. 15315–15320, 2018.
[54] M.-S. Yao *et al.*, "Gold–tin co-sensitized ZnO layered porous nanocrystals: Enhanced responses and anti-humidity," *RSC Adv*, vol. 7, no. 33, pp. 20273–20280, 2017.
[55] Y. Sun, J. Hu, and Y. Zhang, "Visible light assisted trace gaseous NO2 sensor with anti-humidity ability via LSPR enhancement effect," *Sens Actuators B Chem*, vol. 367, p. 132032, 2022.
[56] A. A. Haidry, A. Ebach-Stahl, and B. Saruhan, "Effect of Pt/TiO2 interface on room temperature hydrogen sensing performance of memristor type Pt/TiO2/Pt structure," *Sens Actuators B Chem*, vol. 253, pp. 1043–1054, 2017.
[57] H. Liu, B. Liu, P. Li, W. Kang, and Y. Zhang, "High sensitivity and anti-humidity gas sensor for nitrogen dioxide based on Ce/SnO2 nanomaterials," *Sens Actuators A Phys*, vol. 344, p. 113717, 2022.
[58] Q. Qi *et al.*, "Trimethylamine sensors with enhanced anti-humidity ability fabricated from La0. 7Sr0. 3FeO3 coated In2O3–SnO2 composite nanofibers," *Sens Actuators B Chem*, vol. 203, pp. 111–117, 2014.
[59] Y. Tan *et al.*, "Improving Anti-Humidity Property of a SnO2-Based Chemiresistive Hydrogen Sensor by a Breathable and Hydrophobic Fluoropolymer Coating," *Langmuir*, vol. 38, no. 45, pp. 13833–13840, 2022.
[60] A. Al Shboul, A. Shih, and R. Izquierdo, "A flexible indium oxide sensor with anti-humidity property for room temperature detection of hydrogen sulfide," *IEEE Sens J*, vol. 21, no. 8, pp. 9667–9674, 2020.
[61] J. Liu, L. Zhang, J. Fan, B. Zhu, and J. Yu, "Triethylamine gas sensor based on Pt-functionalized hierarchical ZnO microspheres," *Sens Actuators B Chem*, vol. 331, p. 129425, 2021.
[62] H. Li *et al.*, "Plasmon-enhanced photocatalytic properties of Au/ZnO nanowires," *Appl Surf Sci*, vol. 583, p. 152539, 2022.
[63] H. Wang *et al.*, "N-pentanol sensor based on ZnO nanorods functionalized with Au catalysts," *Sens Actuators B Chem*, vol. 339, p. 129888, 2021.
[64] J. C. C. Fan and J. B. Goodenough, "X-ray photoemission spectroscopy studies of Sn-doped indium-oxide films," *J Appl Phys*, vol. 48, no. 8, pp. 3524–3531, 1977.
[65] G. Wu *et al.*, "The effect of oxygen vacancies in ZnO at an Au/ZnO interface on its catalytic selective oxidation of glycerol," *J Catal*, vol. 377, pp. 271–282, 2019.
[66] J. Zhang, X. Li, Q. Pan, T. Liu, and Q. Wang, "Highly Selective Gas Sensor Based on Litchi-like g-C3N4/In2O3 for Rapid Detection of H2," *Sensors*, vol. 23, no. 1, p. 148, 2023.

[67] N. Jayababu, M. Poloju, J. Shruthi, and M. V. R. Reddy, "NiO decorated CeO 2 nanostructures as room temperature isopropanol gas sensors," *RSC Adv*, vol. 9, no. 24, pp. 13765–13775, 2019.
[68] J. Liu, L. Zhang, J. Fan, B. Zhu, and J. Yu, "Triethylamine gas sensor based on Pt-functionalized hierarchical ZnO microspheres," *Sens Actuators B Chem*, vol. 331, p. 129425, 2021.
[69] P. P. Sahay and R. K. Nath, "Al-doped ZnO thin films as methanol sensors," *Sens Actuators B Chem*, vol. 134, no. 2, pp. 654–659, 2008.
[70] Y. Seekaew, A. Wisitsoraat, D. Phokharatkul, and C. Wongchoosuk, "Room temperature toluene gas sensor based on TiO2 nanoparticles decorated 3D graphene-carbon nanotube nanostructures," *Sens Actuators B Chem*, vol. 279, pp. 69–78, 2019.
[71] D. Zhang, C. Jiang, and Y. Zhang, "Room temperature hydrogen gas sensor based on palladium decorated tin oxide/molybdenum disulfide ternary hybrid via hydrothermal route," *Sens Actuators B Chem*, vol. 242, pp. 15–24, 2017.
[72] S. Brahma, Y.-W. Yeh, J.-L. Huang, and C.-P. Liu, "Cu-doped p-type ZnO nanostructures as unique acetone sensor at room temperature (~ 25 C)," *Appl Surf Sci*, vol. 564, p. 150351, 2021.
[73] Z. Q. Zheng, J. D. Yao, B. Wang, and G. W. Yang, "Light-controlling, flexible and transparent ethanol gas sensor based on ZnO nanoparticles for wearable devices," *Sci Rep*, vol. 5, no. 1, p. 11070, 2015.
[74] Q. Zeng, Y. Cui, L. Zhu, and Y. Yao, "Increasing oxygen vacancies at room temperature in SnO2 for enhancing ethanol gas sensing," *Mater Sci Semicond Process*, vol. 111, p. 104962, 2020.
[75] Q. Xu *et al.*, "Near room-temperature triethylamine sensor constructed with CuO/ZnO PN heterostructural nanorods directly on flat electrode," *Sens Actuators B Chem*, vol. 225, pp. 16–23, 2016.
[76] D.-X. Ju *et al.*, "Near room temperature, fast-response, and highly sensitive triethylamine sensor assembled with Au-loaded ZnO/SnO2 core–shell nanorods on flat alumina substrates," *ACS Appl Mater Interfaces*, vol. 7, no. 34, pp. 19163–19171, 2015.
[77] L.-X. Shan, Y. Li, R.-C. Wang, and X.-X. Lian, "Sensing properties of ZnS@ ZnO core-shell based triethylamine sensor fabricated using solvothermal and sintering methods," *J Alloys Compd*, vol. 944, p. 169223, 2023.
[78] B. Zi *et al.*, "CuO@ In2O3/ZnO Core–Shell Nanorods for Triethylamine Detection at Room Temperature," *ACS Appl Nano Mater*, vol. 6, no. 8, pp. 6963–6971, 2023.
[79] Y. Chen, Z. Wang, H. Fu, D. Han, and F. Gu, "Insights into the effect of Au particle size on triethylamine sensing properties based on a Au–ZnO nanoflower sensor," *J Mater Chem C Mater*, vol. 10, no. 9, pp. 3318–3328, 2022.
[80] S. Li, Y. Zhang, L. Han, X. Li, and Y. Xu, "Highly sensitive and selective triethylamine gas sensor based on hierarchical radial CeO2/ZnO nn heterojunction," *Sens Actuators B Chem*, vol. 367, p. 132031, 2022.
[81] C. Dong *et al.*, "Anchoring Pt particles onto mesoporousized ZnO holey cubes for triethylamine detection with multifaceted superiorities," *Small*, p. 2300756, 2023.
[82] S. Zhang, P. Song, Q. Wang, and Y. Ding, "Ultra-sensitive triethylamine gas sensor based on ZnO/MoO3 heterostructures with ppb level detection," *Sens Actuators B Chem*, vol. 379, p. 133239, 2023.

[83] J. Fang, J.-J. Xue, R.-P. Xiao, X. Chen, Y.-M. Guo, and J.-M. Song, “Synthesis of Pr-doped ZnO nanospindles by one-pot precipitation as a triethylamine sensor,” *J Environ Chem Eng*, vol. 10, no. 5, p. 108334, 2022.